

A wireless closed-loop system for optogenetic peripheral neuromodulation

Aaron D. Mickle^{1,2,17}, Sang Min Won^{3,17}, Kyung Nim Noh^{3,17}, Jangyeol Yoon^{4,17}, Kathleen W. Meacham^{1,2}, Yeguangu Xue^{5,6,7}, Lisa A. McIlvried^{1,2}, Bryan A. Coptis^{1,2}, Vijay K. Samineni^{1,2}, Kaitlyn E. Crawford⁸, Do Hoon Kim⁴, Paulome Srivastava^{1,2}, Bong Hoon Kim^{4,7,9,10}, Seunghwan Min⁴, Young Shiuian^{1,2}, Yeojeong Yun⁴, Maria A. Payne^{2,11}, Jianpeng Zhang¹², Hokyung Jang⁴, Yuhang Li¹², H. Henry Lai^{1,2,11}, Yonggang Huang^{5,6,7}, Sung-Il Park¹³, Robert W. Gereau IV^{1,2*} & John A. Rogers^{4,6,7,9,10,14,15,16*}

The fast-growing field of bioelectronic medicine aims to develop engineered systems that can relieve clinical conditions by stimulating the peripheral nervous system^{1–5}. This type of technology relies largely on electrical stimulation to provide neuromodulation of organ function or pain. One example is sacral nerve stimulation to treat overactive bladder, urinary incontinence and interstitial cystitis (also known as bladder pain syndrome)^{4,6,7}. Conventional, continuous stimulation protocols, however, can cause discomfort and pain, particularly when treating symptoms that can be intermittent (for example, sudden urinary urgency)⁸. Direct physical coupling of electrodes to the nerve can lead to injury and inflammation^{9–11}. Furthermore, typical therapeutic stimulators target large nerve bundles that innervate multiple structures, resulting in a lack of organ specificity. Here we introduce a miniaturized bio-optoelectronic implant that avoids these limitations by using (1) an optical stimulation interface that exploits microscale inorganic light-emitting diodes to activate opsins; (2) a soft, high-precision biophysical sensor system that allows continuous measurements of organ function; and (3) a control module and data analytics approach that enables coordinated, closed-loop operation of the system to eliminate pathological behaviours as they occur in real-time. In the example reported here, a soft strain gauge yields real-time information on bladder function in a rat model. Data algorithms identify pathological behaviour, and automated, closed-loop optogenetic neuromodulation of bladder sensory afferents normalizes bladder function. This all-optical scheme for neuromodulation offers chronic stability and the potential to stimulate specific cell types.

This fully implantable, wireless neuromodulation system combines a thin, low-modulus strain gauge to monitor bladder filling and voiding with microscale inorganic light-emitting diodes (μ -ILEDs) to control inhibitory opsins expressed virally in bladder sensory afferents. To achieve the desired closed-loop control of bladder dysfunction, the entire integrated platform includes five interconnected sub-systems: (1) a low-modulus, stretchable strain gauge that encircles the bladder to measure bladder activity (filling and voiding); (2) a pair of μ -ILEDs that deliver light directly to the bladder for optogenetic neuromodulation; (3) a thin, soft base station that is inserted between the abdominal skin and muscle for bidirectional communication and wireless control of the μ -ILED actuators; (4) a wireless harvesting unit that distributes power to the entire system; and (5) customized software deployed on a handheld device to enable real-time visualization, storage and analysis of operational data, and to provide an automated control interface for

setting illumination protocols and parameters for open- or closed-loop interventions (Fig. 1a, b). Sub-systems 1–4 integrate into two separate modules (sub-systems 1–2 and 3–4) that are electrically connected within the body of the rat by insulated fine wires. This system provides a critical advantage over other real-time bladder function measurements in that it does not demand direct nerve interfaces or incisions in the bladder, as required for most pressure-monitoring approaches. Implantation of sub-systems 1 and 2, referred to as the optoelectronic stimulation and sensing module, involves a conformal circumferential interface between the strain gauge and the bladder, secured by an integrated buckle with a small dissolvable suture to the detrusor muscle (Extended Data Fig. 1a, b). Sub-systems 3 and 4, referred to as the wireless control and power (WCP) module, is a thin, flexible component that inserts subcutaneously into the abdomen (Fig. 1c, d). One month after implantation, the optoelectronic stimulation and sensing module and WCP module both remained in their original positions (Fig. 1e), with no signs of degradation in functionality or performance.

The optoelectronic stimulation and sensing module combines a thin ($15\text{-}\mu\text{m}$) layer of silicone doped with carbon black as a resistive strain gauge, with a pair of μ -ILEDs for optogenetic stimulation (Fig. 2a and Extended Data Fig. 2a). A low-modulus silicone material serves as the substrate and provides overall encapsulation. The entire platform encircles the bladder, such that dimensional changes in the bladder that occur with filling stretch the strain gauge. The resulting changes in resistance correlate with bladder volume (Extended Data Fig. 2b, c). The shape of the optoelectronic stimulation and sensing module and its low-modulus construction allow reliable chronic function and durable detection of bladder expansion or contraction (Extended Data Fig. 2d, e). While the strain–stress curves obtained by dynamic mechanical analysis indicate that the modulus of the responsive material in the strain gauge is 270 kPa, the overall modulus of the strain gauge device is much lower, at 70 kPa (Fig. 2b). This result follows from a design in which the narrow strain gauge (thickness $15\text{ }\mu\text{m}$) rests between two layers of undoped silicone film (thickness $40\text{ }\mu\text{m}$, modulus 60 kPa) (Extended Data Fig. 2f). Finite element analysis (FEA) of experimental measurements of changes in bladder dimensions caused by filling with saline (Extended Data Fig. 2g–i) suggests that the modulus of the bladder wall is between 10 and 40 kPa, from empty to full, consistent with previous reports¹². These modulus values allow FEA simulations of the bladder radius, assuming a spheroidal shape, during expansion with and without the strain gauge (Fig. 2c, d). Deformations of the bladder due to the strain gauge are less than 2% of overall expansion due to filling, consistent with negligible mechanical loading. In vivo measurements

¹Washington University Pain Center and Department of Anesthesiology, Washington University, St Louis, MO, USA. ²Washington University School of Medicine, St Louis, MO, USA. ³Department of Electrical and Computer Engineering, University of Illinois at Urbana-Champaign, Urbana, IL, USA. ⁴Department of Materials Science and Engineering, University of Illinois at Urbana-Champaign, Urbana, IL, USA. ⁵Department of Civil and Environmental Engineering, Northwestern University, Evanston, IL, USA. ⁶Mechanical Engineering, Northwestern University, Evanston, IL, USA. ⁷Materials Science and Engineering, Northwestern University, Evanston, IL, USA. ⁸Department of Materials Science and Engineering, University of Central Florida, Orlando, FL, USA. ⁹Simpson Querrey Institute, Northwestern University, Chicago, IL, USA. ¹⁰Center for Bio-integrated Electronics, Northwestern University, Evanston, IL, USA. ¹¹Washington University Department of Surgery - Division of Urologic Surgery, St Louis, MO, USA. ¹²Institute of Solid Mechanics, Beihang University (BUAA), Beijing, China. ¹³Department of Electrical and Computer Engineering, Texas A&M University, College Station, TX, USA. ¹⁴Department of Biomedical Engineering, Northwestern University, Evanston, IL, USA. ¹⁵Department of Chemistry, Northwestern University, Evanston, IL, USA. ¹⁶Department of Neurological Surgery, Feinberg School of Medicine, Northwestern University, Chicago, IL, USA. ¹⁷These authors contributed equally: Aaron D. Mickle, Sang Min Won, Kyung Nim Noh, Jangyeol Yoon. *e-mail: gereaur@wustl.edu; jrogers@northwestern.edu

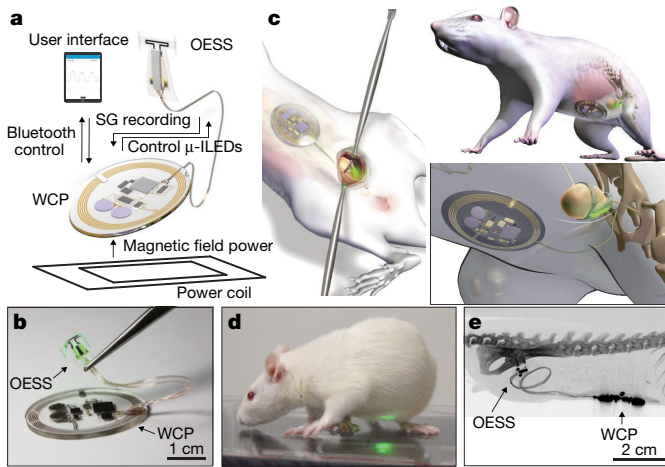


Fig. 1 | Schematic illustrations and images of a fully implantable, soft optoelectronic system for wireless, closed-loop optogenetic modulation of bladder function. **a**, The platform consists of an optoelectronic stimulation and sensing (OESS) module and a low-modulus, stretchable strain gauge (SG) with integrated μ -ILEDs that wraps around the bladder to monitor changes in its volume and to provide optogenetic stimulation to the neurons that innervate the bladder. The WCP module records the response of the strain gauge, controls operation of the μ -ILEDs and provides power management. Wireless data communication to and from the WCP module relies on Bluetooth protocols and a tablet computer. Power is delivered wirelessly by resonant magnetic coupling through an antenna transmitter. **b**, Photograph of optoelectronic stimulation and sensing module including the strain gauge, μ -ILEDs and wireless base station for data communication. **c**, Schematic illustrations showing the placement of the strain gauge around the bladder, with an implanted, wired connection to the WCP module subcutaneously implanted anterior to the bladder. Images created by and used with permission of Janet Sinn-Hanlon, The DesignGroup@VetMed, University of Illinois at Urbana-Champaign. **d**, Rat implanted with the complete system (a green μ -ILED indicator on the WCP module verifies function). **e**, Computed tomography image of a device implanted for 1 month.

of cystometric pressures during filling and voiding show no effects of the device, consistent with the results of FEA (Fig. 2e).

The μ -ILEDs mount on a thin (25 μ m), flexible substrate of stainless steel and exploit transparent layers of polyisobutylene and polydimethylsiloxane as front-side encapsulation (Extended Data Fig. 3a). Activation of the μ -ILEDs causes $44 \pm 11 \mu$ W of light (540 nm) to pass through the full-thickness (non-stretched) bladder wall (Extended Data Fig. 3b, c). The small dimensions of the μ -ILEDs and the high thermal conductivity of the stainless steel result in efficient dissipation of thermal load associated with operation, even under continuous illumination. Measurements indicate that one hour of constant illumination leads to an increase of less than 1 °C in the temperature of the contacting tissue (Extended Data Fig. 3d–h).

To communicate strain gauge sensor readings to a user interface, the WCP module incorporates a low-powered radio frequency-embedded microcontroller and wireless power management circuitry (Fig. 2f, g and Extended Data Fig. 4a). Power passes to the WCP module wirelessly via resonant inductive coupling through a three-coil wireless power transfer link. The transmitter side incorporates a 13.56-MHz radio frequency identification driver, impedance-matching circuitry, and a primary coil. A secondary resonating coil wrapped around the bottom of the cage to enhance the efficiency of power transfer, and a load coil in the WCP module constitute the receiver end (Extended Data Fig. 4b). Matching the impedance of the receiver coils such that they resonate at 13.56 MHz yields a loosely coupled wireless power transfer system, designed to alleviate sensitivities to mismatches in antenna characteristics and allow wireless power transfer coverage throughout the rat cage. The received voltage on the parallel-resonant load coil is rectified with a full-bridge rectifier and regulated using a

charge pump converter to simultaneously power the wireless system and charge a pair of supercapacitors within the WCP module. These supercapacitors act as a short-term energy buffer (two 3.3-V, 80-mF supercapacitors) during periods when the wirelessly received power is insufficient to operate the system; such periods are typically caused by rotations of the animal (most commonly, rearing for 1–5 s) that lead to an angular mismatch between the load antenna on the WCP module and the primary transmission antenna (Extended Data Fig. 4c). The supercapacitors can power the system for more than 3 min without external power (Extended Data Fig. 4d); wireless charging occurs in about 30 s when the transmitting antenna outputs 4 W.

The full closed-loop optogenetic control (CLOC) system accurately monitors bladder activity, where large decreases in resistance (decreases in bladder size) correlate with voiding events as measured by a metabolic cage (Fig. 3a). Notably, implantation of the CLOC system did not significantly affect the cystometric properties of the bladder 7 days after implantation, compared to rats that underwent sham implantation surgery (Extended Data Fig. 5a, b). This finding confirms that the strain gauge does not constrict the bladder, and that there is no significant formation of fibrosis around the bladder, which could decrease bladder compliance. In addition, no significant inflammatory responses, alterations to gait, movement or weight changes were observed 7 days after device implantation, compared to rats that underwent sham surgery (Extended Data Fig. 5c–h). Together, these results indicate that the implanted CLOC system accurately measures bladder function, has minimal effect on bladder physiology, and does not cause detectable harm or distress to the animal.

An optogenetic strategy allows modulation of bladder function, enabled by injection of a herpes-simplex viral (HSV) vector containing a genetic payload to express the inhibitory opsin archaerhodopsin 3.0 (Arch)¹³ (tagged with enhanced yellow fluorescent protein (eYFP)) directly into the bladder wall. This approach enables specific neuromodulation of sensory afferents that innervate the bladder, as differentiated from traditional electric stimulation of the sacral root, which also activates neurons that innervate the colon and other pelvic structures. Because HSV vectors provide tropism for sensory neurons¹⁴, this injection results in the expression of Arch in sensory neurons that innervate the bladder; Arch protein was detectable in peripheral terminals in the bladder wall, as well as cell bodies of dorsal root ganglion (DRG) neurons, 7 days after injection (Fig. 3b). Injection of viral vectors alone did not significantly alter cystometric properties or cause alterations in mast cell degranulation, a marker for inflammatory response, 7 days after injection (Extended Data Fig. 6). Isolated bladder-projecting DRG neurons transduced with Arch–eYFP demonstrated reduced neuronal excitability on exposure to 530 nm light (Extended Data Fig. 7a–e). In addition, Arch activation reduced neuronal excitability in DRGs cultured from human donors and transduced with Arch–eYFP (Extended Data Fig. 7e–k). Together, these results illustrate that HSV vectors transduce the inhibitory opsin Arch into bladder-projecting sensory neurons without overt tissue damage, and that activation of Arch in rat or human DRG neurons decreases neuronal excitability.

Anaesthetized cystometry, a measure of the physiological properties of the bladder, reveals the effects of Arch-mediated neuronal inhibition on bladder function. In rats that express Arch–eYFP in bladder-projecting neurons, illumination of the bladder significantly increased the intercontraction interval (ICI) compared to rats expressing only eYFP (Extended Data Fig. 8a, b), as demonstrated using an implanted optoelectronic stimulation and sensing module ($P = 0.008$) and intravesicular catheters to measure bladder pressure ($P = 0.007$). These groups, however, showed no differences in peak, baseline, or threshold pressures (Extended Data Fig. 8c). Similar degrees of ICI delay appeared in data collected using the strain gauges and intravesicular pressure sensors, providing further evidence that the optoelectronic stimulation and sensing module accurately measures bladder function.

Implantation of CLOC platforms in rats that express Arch–eYFP or eYFP allowed assessments of the effect of Arch activation on normal voiding in awake, freely moving rats. Bladder illumination did not alter

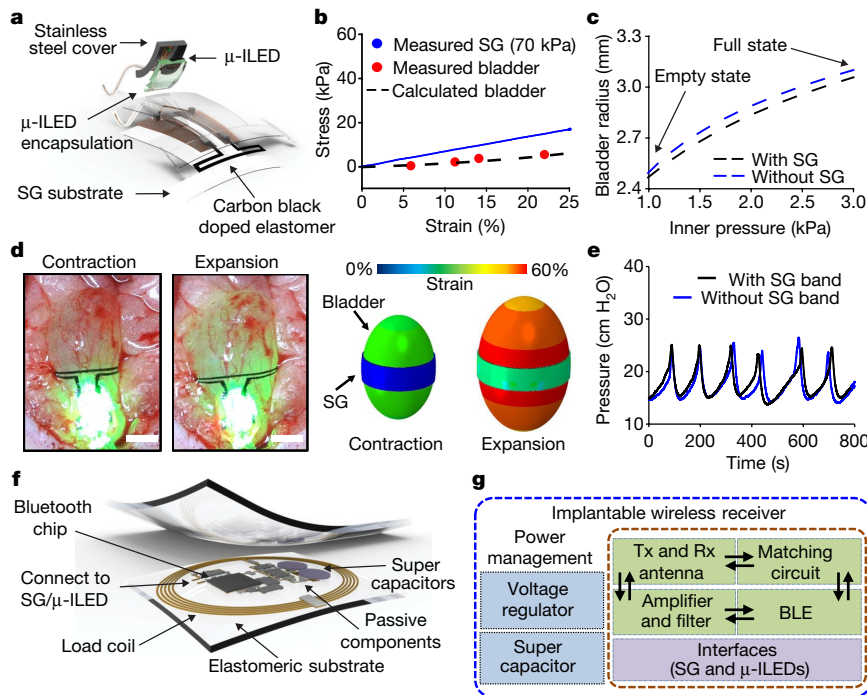


Fig. 2 | Electrical and mechanical properties of the optoelectronic stimulation and sensing module. **a**, Schematic illustration of the optoelectronic stimulation and sensing module. **b**, Dynamic mechanical analysis of a strain gauge with comparison to a simulated stress-strain curve of bladder from the empty state. **c**, Simulated radius of a bladder during expansion with and without an integrated optoelectronic stimulation and sensing module. **d**, Left, images of a strain gauge and a pair of μ -ILEDs wrapped around the outer surface of the rat bladder, in

contracted and expanded states. Right, computed distributions of strain for a strain gauge integrated with a spheroidal model of the rat bladder. Scale bars, 2.5 mm. **e**, Acute rat bladder cystometry before and after placement of the optoelectronic stimulation and sensing module, demonstrating no discernable alterations to intravesical pressure. **f**, Schematic illustration of the implantable WCP module. **g**, Operational block diagram of the overall system design. BLE, Bluetooth Low Energy; Rx, receiving; Tx, transmitting.

void frequency, or the time to first void during the 3-h illumination period, in Arch-eYFP/LED-ON, eYFP/LED-ON and virus-injected/LED-OFF groups (Extended Data Fig. 8d). Rats previously treated with cyclophosphamide (CYP, 75 mg kg⁻¹ by intraperitoneal (IP) injection) to induce voiding dysfunction¹⁵ showed significant increases in the frequency of voiding ($P = 0.008$) and time to first void ($P = 0.002$) but no significant increase in bladder nociception (Extended Data Fig. 8e, f). Thus, under the present experimental conditions it was not possible to determine whether the system could also reduce cystitis-induced increases in bladder pain. In CYP-injected rats, bladder illumination resulted in a significant decrease in the number of voids in the Arch-eYFP/LED-ON group compared to eYFP/LED-ON ($P = 0.025$) and virus-injected/LED-OFF ($P = 0.032$) groups during the 3 h after injection (Fig. 3c, d). In addition, there was a significant increase in the time to the first void after CYP injection in the Arch-eYFP/LED-ON group compared to the eYFP/LED-ON ($P = 0.038$) and virus-injected/LED-OFF groups ($P = 0.009$) (Fig. 3d).

Fully automated use of the CLOC system requires algorithmic identification of strain gauge data signatures of abnormal bladder voiding. Real-time signal processing methods classify abnormal bladder activity on the basis of identification of voiding events, indicated by relatively prolonged increases in strain gauge resistance (increases in bladder size) followed by rapid decreases (rapid decreases in bladder size). Further, void volume can be estimated by evaluating the change in resistance during the voiding event. Preliminary 'training' data from the strain gauge collected concurrently with data from the metabolic cage facilitate the development of signal processing methods that accurately differentiate voiding events from noise due to motion artefacts or other parasitic signals. Voiding events were identified by filtering the raw strain gauge data (1 Hz sampling rate) with a 60-point moving average, down-sampling the results to 0.25 Hz, and then computing the derivative of these processed data (Extended Data Fig. 9a). These steps suppress high-frequency noise associated with non-voiding events, such

as internal organ movement and motion artefacts, but retain voiding data, which occur on timescales of 10–30 s. Analysis of these data shows that voiding events correlate strongly with three consecutive values of the derivatives that are less than a pre-set threshold. The value of this pre-set threshold corresponds to the standard deviation of 1 h of strain gauge data, collected on each animal or device, to account for device-to-device and animal-to-animal variability. A final step rejects identified voids as false if they occurred shortly after instances of large rapid increases in the strain gauge response, a movement artefact that would represent a non-feasible bladder expansion. Altogether, this algorithm identifies voids with more than 85% accuracy in naive rats and with more than 95% accuracy after induction of abnormal voiding with CYP (Extended Data Fig. 9b).

Analysis of the training data set indicates that, in the context of CYP-induced cystitis, frequency (all animals showed a greater than twofold increase in voids after CYP) is a more consistent indicator of the disease state than change in void size (Extended Data Fig. 9c). We therefore consider only a change in void frequency (to three voids within 1 h) as the beginning of the disease condition. However, in different contexts it might be critical to assess volume, so we include an additional feature within the software to evaluate void volume compared to a threshold. If a void is larger than the threshold, it is considered a 'healthy' void, and is not counted towards closed-loop activation. We validated this functionality with an in vitro model, in which larger simulated voids did not activate the closed-loop system regardless of the intervals, whereas frequent smaller voids could activate the μ -ILED (Extended Data Fig. 9d).

Closed-loop operation involves the execution of a software application that enables real-time processing of the signal, logging of responses of the strain gauge for subsequent analysis, activation or deactivation of the μ -ILEDs and implementation of the analysis algorithms described above. The application also includes a user interface to define variables that include derivative thresholds for identifying voiding events. When the patterns of voiding meet the criteria defined by these input values

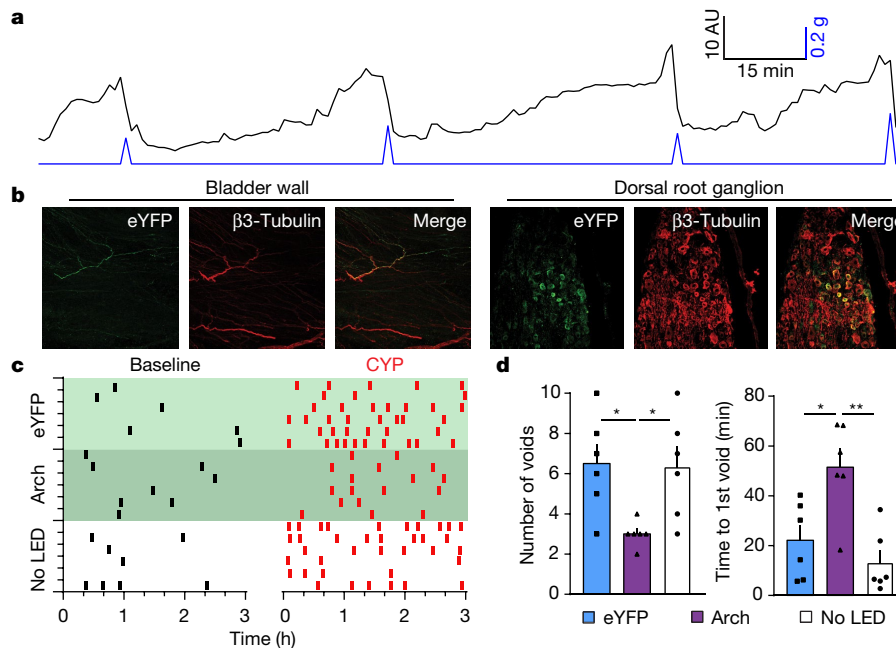


Fig. 3 | Optogenetic modulation of bladder function. **a**, Time dependence of strain gauge data (black; 60-point running average) collected from a freely moving rat implanted with a CLOC system, showing rapid decreases in resistance that correlate with micturition events measured by a computerized balance in a micturition cage (blue). AU, arbitrary units. **b**, Expression of Arch-eYFP in bladder afferent endings and cell bodies of the DRG 7 days after injection of HSV-

(three voids per hour, as informed by our training data), the μ -ILEDs activate for 2 h (Fig. 4a).

Seven days after viral transduction of Arch-eYFP or eYFP and implantation of the CLOC system, the closed-loop software was initiated. The system does not activate the μ -ILEDs before injection of CYP (150 mg kg^{-1} , IP) (Fig. 4b). Activation results in a reduction in the frequency of voiding in the Arch-eYFP-transduced animals compared to the eYFP controls, similar to the experimenter-initiated μ -ILED experiments (Fig. 3c, d). These results demonstrate that the CLOC system can automatically recognize abnormal voiding patterns using algorithmic detection of voiding events and that conditional activation of μ -ILEDs can attenuate this CYP-induced increase in voiding.

In summary, the fully wireless, implantable bio-optoelectronics systems reported here represent a class of technology that allows

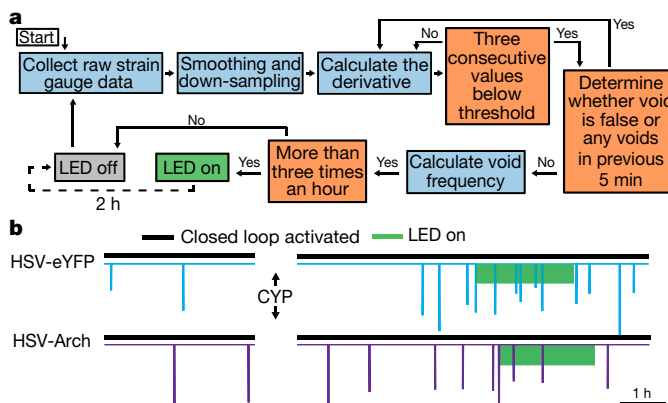


Fig. 4 | Closed-loop optogenetic control of bladder function. **a**, Flow chart of the steps implemented in the closed-loop software to activate the μ -ILED when voiding becomes hyperactive. **b**, Demonstration of closed-loop μ -ILED activation, initiated at an average of 265 min after injection of CYP with corresponding decrease in voiding events in rats injected with HSV-Arch-eYFP compared to control rats injected with HSV-eYFP.

Arch-eYFP into the bladder wall. **c**, Raster plot representing voiding of individual rats (horizontal rows) before and after injection of CYP in HSV-eYFP/LED-ON, HSV-Arch-eYFP/LED-ON and virus-injected/LED-OFF groups before and after CYP injection. **d**, Quantification of mean number of voids 3 h after CYP injection and time to first void after CYP injection in all groups. $n = 6$ rats per group; * $P < 0.05$, ** $P < 0.01$; two-way ANOVA with Tukey's multiple comparison test; mean \pm s.e.m.

closed-loop modulation of peripheral organ function by combined, coordinated operation of a soft, biophysical sensor for feedback control and a proximal light source for optogenetic stimulation. The results illustrate that the approach of using virally delivered opsins as peripheral nervous system (PNS) neuromodulators^{16–22} can be effective for normalization of bladder dysfunction in freely moving animals. Further extension of this work could utilize excitatory opsins to stimulate bladder contractions in the context of underactive bladder. Our prior work in mice¹⁵ and preliminary data in rats suggest that voiding can be enhanced using a similar optogenetic approach. However, further refinement of viral targeting strategies would be necessary to avoid targeting nociceptive afferents and thus causing pain.

As evidence of the potential translatability of this viral approach, we note that Arch activation can successfully decrease the excitability of human DRG neurons in a manner similar to that shown in rats (Extended Data Fig. 7). Initial clinical trials using opsins are underway^{23,24}, but demonstration of the safety and efficacy of chronic opsin expression is needed to realize the full therapeutic potential of optogenetic neuromodulation. Furthermore, light delivery technology would need to be scaled to provide adequate illumination to the much thicker and larger volumes of tissue in the human bladder.

Although the current study demonstrates the utility of this approach in monitoring and modulating bladder function, the core ideas and the supporting technology platforms can be easily adapted to address a range of application possibilities beyond those associated with the bladder. For example, the optoelectronic stimulation and sensing module can be modified to integrate multiple biophysical (temperature, flow, pressure, and so on) and/or biochemical (metabolites, proteins, hormones, and so on) sensors, and can be configured with various types of actuators (such as optical, electrical, pharmacological) to provide the desired modulation, all using control provided by adapted forms of the WCP module and data analytics approaches at the software level. In this sense, the platforms introduced here have versatile uses in pre-clinical and clinical studies into the physiology and pathophysiology of the PNS. Together, this system and our supporting demonstration studies provide a framework for future closed-loop technologies suitable

for treatment of diseases affecting the PNS, offering alternatives to non-specific pharmacological or electrical stimulation approaches.

Online content

Any Methods, including any statements of data availability and Nature Research reporting summaries, along with any additional references and Source Data files, are available in the online version of the paper at <https://doi.org/10.1038/s41586-018-0823-6>.

Received: 26 June 2018; Accepted: 14 November 2018;

Published online 2 January 2019.

- Birmingham, K. et al. Bioelectronic medicines: a research roadmap. *Nat. Rev. Drug Discov.* **13**, 399–400 (2014).
- Cameron, T. Safety and efficacy of spinal cord stimulation for the treatment of chronic pain: a 20-year literature review. *J. Neurosurg.* **100**, 254–267 (2004).
- De Ferrari, G. M. et al. Chronic vagus nerve stimulation: a new and promising therapeutic approach for chronic heart failure. *Eur. Heart J.* **32**, 847–855 (2011).
- de Groat, W. C. & Tai, C. Impact of bioelectronic medicine on the neural regulation of pelvic visceral function. *Bioelectron. Med.* **2015**, 25–36 (2015).
- Famm, K., Litt, B., Tracey, K. J., Boyden, E. S. & Slaoui, M. Drug discovery: a jump-start for electroceuticals. *Nature* **496**, 159–161 (2013).
- Janknegt, R. A. et al. Long-term effectiveness of sacral nerve stimulation for refractory urge incontinence. *Eur. Urol.* **39**, 101–106 (2001).
- Siegel, S. W. et al. Long-term results of a multicenter study on sacral nerve stimulation for treatment of urinary urge incontinence, urgency-frequency, and retention. *Urology* **56**, 87–91 (2000).
- Kavvadias, T., Huebner, M., Brucker, S. Y. & Reisenauer, C. Management of device-related complications after sacral neuromodulation for lower urinary tract disorders in women: a single center experience. *Arch. Gynecol. Obstet.* **295**, 951–957 (2017).
- del Valle, J. & Navarro, X. Interfaces with the peripheral nerve for the control of neuroprostheses. *Int. Rev. Neurobiol.* **109**, 63–83 (2013).
- Rossini, P. M. et al. Double nerve intraneural interface implant on a human amputee for robotic hand control. *Clin. Neurophysiol.* **121**, 777–783 (2010).
- Yoshida, K., Farina, D., Akay, M. & Jensen, W. Multichannel intraneural and intramuscular techniques for multiunit recording and use in active prostheses. *Proc. IEEE* **98**, 432–449 (2010).
- Miftahof, R. & Nam, H. G. *Biomechanics of the Human Urinary Bladder* (Springer, 2013).
- Mattis, J. et al. Principles for applying optogenetic tools derived from direct comparative analysis of microbial opsins. *Nat. Methods* **9**, 159–172 (2012).
- Zerboni, L. et al. Herpes simplex virus 1 tropism for human sensory ganglion neurons in the severe combined immunodeficiency mouse model of neuropathogenesis. *J. Virol.* **87**, 2791–2802 (2013).
- DeBerry, J. J. et al. Differential regulation of bladder pain and voiding function by sensory afferent populations revealed by selective optogenetic activation. *Front. Integr. Neurosci.* **12**, 5 (2018).
- Beaudry, H., Daou, I., Ase, A. R., Ribeiro-da-Silva, A. & Séguéla, P. Distinct behavioral responses evoked by selective optogenetic stimulation of the major TRPV1⁺ and MrgD⁺ subsets of C-fibers. *Pain* **158**, 2329–2339 (2017).
- Boada, M. D. et al. Fast-conducting mechanoreceptors contribute to withdrawal behavior in normal and nerve injured rats. *Pain* **155**, 2646–2655 (2014).
- Iyer, S. M. et al. Virally mediated optogenetic excitation and inhibition of pain in freely moving nontransgenic mice. *Nat. Biotechnol.* **32**, 274–278 (2014).
- Iyer, S. M. et al. Optogenetic and chemogenetic strategies for sustained inhibition of pain. *Sci. Rep.* **6**, 30570 (2016).
- Li, B. et al. A novel analgesic approach to optogenetically and specifically inhibit pain transmission using TRPV1 promoter. *Brain Res.* **1609**, 12–20 (2015).
- Montgomery, K. L. et al. Wirelessly powered, fully internal optogenetics for brain, spinal and peripheral circuits in mice. *Nat. Methods* **12**, 969–974 (2015).
- Towne, C., Montgomery, K. L., Iyer, S. M., Deisseroth, K. & Delp, S. L. Optogenetic control of targeted peripheral axons in freely moving animals. *PLoS One* **8**, e72691 (2013).
- ClinicalTrials.gov. RST-001 phase I/II trial for advanced retinitis pigmentosa. <https://ClinicalTrials.gov/show/NCT02556736> (2018).
- ClinicalTrials.gov. Dose-escalation study to evaluate the safety and tolerability of GS030 in subjects with retinitis pigmentosa. <https://ClinicalTrials.gov/show/NCT03326336> (2018).

Acknowledgements We acknowledge the generosity of the donor families, as well as Mid-America Transplant for making the studies of human sensory neurons possible. J. Lemen provided instrumental help during human DRG surgical extractions. We thank J. Sinn-Hanlon for the illustrations, L. Strong for technical assistance with the CT imaging, S. Vogt for technical support and C. Morgan for early input on the project. This work was funded by an NIH Director's Transformative Research Award TR01 NS081707 (R.W.G. and J.A.R.), an NIH SPARC Award via the NIBIB of the NIH U18 EB021793 (R.W.G. and J.A.R.), R01 NS42595 (R.W.G.), NRSA F32 DK115122 (A.D.M.), the McDonnell Center for Cellular and Molecular Neurobiology Postdoctoral Fellowship (A.D.M.), K01 DK115634 (V.K.S.), the Urology Care Foundation Research Scholars Program and Kailash Kedia Research Scholar Endowment (V.K.S.), NSF Grant 1635443 (Y.H.), the Ryan Fellowship and the Northwestern University International Institute for Nanotechnology (Y.X.), T32 DA007261 (L.A.M.), T32 DK108742 (K.W.M.), T32 GM 108539 (B.A.C.), Washington University BioSURF Fellowship (P.S.) DK082315 (H.H.L.) and K08 DK094964 (H.H.L.).

Reviewer information Nature thanks T. Chai, C. Moritz, E. Roche and S. Zderic for their contribution to the peer review of this work.

Author contributions A.D.M., S.M.W., K.N.N. and J.Y. contributed equally to the work; A.D.M., S.M.W., K.N.N., K.W.M., J.Y., S.-I.P., J.A.R. and R.W.G. conceived of and designed experiments and material devices; S.M.W., K.N.N., J.Y., K.E.C., B.H.K., S.M., D.H.K., Y.Y., H.J. and S.-I.P. designed and provided optoelectronic devices; S.M.W., K.N.N. and J.Y. conducted all bench top tests; S.M.W. provided device illustration; Y.X., J.Z., Y.L., and Y.H. contributed to mechanical and thermal simulations; A.D.M. performed all surgical implantations and viral injections; A.D.M., L.A.M., P.S. and Y.S. collected and analysed histological data; A.D.M. performed and analysed data from cytometry stain gauges and gait analysis; V.K.S. collected and analysed data from open field experiments; M.A.P. collected and analysed VMR data; L.A.M. and B.A.C. collected and analysed data from the electrophysiology experiments; A.D.M., S.M.W. and K.N.N. designed and tested the closed-loop algorithm; K.N.N. programmed and tested the iOS software; H.H.L. provided guidance and resources for cystometric and metabolic studies; and A.D.M., S.M.W., K.N.N., J.A.R. and R.W.G. wrote the manuscript.

Competing interests J.A.R. and R.W.G. are co-founders of Neurolux, a company that manufactures wireless optoelectronic devices. The device described here uses similar technology, but is distinct from the current Neurolux portfolio.

Additional information

Extended data is available for this paper at <https://doi.org/10.1038/s41586-018-0823-6>.

Supplementary information is available for this paper at <https://doi.org/10.1038/s41586-018-0823-6>.

Reprints and permissions information is available at <http://www.nature.com/reprints>.

Correspondence and requests for materials should be addressed to R.W.G. or J.A.R.

Publisher's note: Springer Nature remains neutral with regard to jurisdictional claims in published maps and institutional affiliations.

METHODS

Fabrication of the wireless control and power module. The first step involved spin-casting a polyimide (PI) film on a copper foil. Laminating the sheet, with the PI side down, onto a glass slide coated with polydimethylsiloxane (PDMS) enabled patterning of the copper layer into a coil geometry by photolithography (photoresist AZ 4620; spin-casting at 3,000 r.p.m. for 30 s, baking on a hot plate at 110 °C for 3 min, UV irradiance for 300 mJ cm⁻², and development for ~40 s with developer AZ 400K/deionized water solution of 1:3 volume ratio) and wet etching (CE-100 copper etchant, Transense; ~2 min with frequent rinsing by water). Dry etching (reactive-ion etching; 20 sccm O₂, 200 mTorr, 150 W, 1,800 s) removed the PI everywhere except underneath the copper traces. A cellulose-based, water-soluble tape (for example, Aquasol Corporation, ASWT-2) allowed retrieval of the structure from the PDMS/glass substrate. Deposition of a bilayer of Ti/SiO₂ onto the back side of the structure allowed covalent bonding to a base layer of PDMS following exposure of the PDMS layer to ultraviolet-induced ozone (UVO). Here, the PDMS surface and ultraviolet lamp in the UVO cleaner chamber (144AX, Jelight Company Inc.) were maintained at a distance of 1 cm apart during a treatment time of 7 min. After we removed the water-soluble tape, solder joints formed between the electronic components and corresponding bond pads on the Cu/PI platform yielded functional systems. Layers of polyisobutylene (PIB) and PDMS were used for encapsulation.

Fabrication of the optoelectronic stimulating component. Extended Data Fig. 3a presents a schematic cross-sectional illustration and layout of the μ -ILEDs. Solder joints and epoxy electrically and mechanically bonded two μ -ILEDs (TR2227, Cree) onto a polyimide substrate with exposed traces of copper. A similar strategy bonded a pair of copper wires in a polyurethane tube (PU-025, SAI infusion technologies) onto copper metal pads at the opposite end of the polyimide substrate to serve as the interconnection between the μ -ILEDs and the WCP module. This component was mounted onto a stainless-steel casing with epoxy (Loctite epoxy marine) coated on the back side. Dip coating followed by a thermal curing process step formed an encapsulating layer of PIB (two coats) and PDMS (three coats) on the light-illuminating anterior, or bladder-facing side, of the optoelectronic stimulation and sensing module.

Fabrication of the strain gauge component. Extended Data Fig. 2a presents a schematic cross-sectional illustration and layout of the SG. A thin layer of silicone elastomer (Ecoflex-0030, 40- μ m thickness) on a water-soluble film of poly(vinyl alcohol) served as a support for a piece of screen-printed silicone doped with carbon black (XC-72R, Fuel Cell Store) at 15% by weight. This carbon-black strain gauge is conceptually similar to ones previously described^{25,26}. Patterns of copper formed on the polyimide substrate, attached to the carbon black-doped silicone ends, provided means for electrical measurement. Silver (H20E Epo-Tek, TExtended Data PELLA) paste and epoxy (Loctite epoxy marine) mechanically and electrically secured the junctions. A spin-cast overcoat of silicone provided encapsulation. A mechanical cutting process defined the final shape of the device. Mechanical bench tests confirmed the strain gauge functionality and durability after repeated mechanical deformation (Extended Data Fig. 10).

Experimental subjects. Adult (200–300 g) female Sprague-Dawley rats (Taconic) housed in pairs with access to food and water ad libitum were maintained on a 12 h:12 h light:dark cycle (lights on at 6:00). All procedures unless specifically stated were performed during the light phase. All experimental procedures were approved by the Animal Care and Use Committee of Washington University and in strict accordance with the United States National Institute of Health (NIH) Guide for the Care and Use of Laboratory Animals.

Surgical implantation of the optoelectronic device. The whole device was first sterilized using ethylene gas, then the optoelectronic stimulation and sensing module was implanted around the bladder with the μ -ILEDs facing the bladder. The strain gauge was secured around the bladder with the lower band (Extended Data Fig. 1b (1–3)). Kwik-Sil adhesive (World Precision Instruments) was used to secure the strap to the base of the device (near the μ -ILEDs), then the top buckle was passed through the connective tissue on the back of the bladder and connected to the other side of the T-shaped buckle (Extended Data Fig. 1b (4)). A small absorbable suture (Plain Gut 6-0, Covidien) was placed through the band and into the smooth muscle layer of the bladder, being careful not to puncture into the bladder lumen (Extended Data Fig. 1b (4, 5)). The wires connecting to the WCP module were then externalized through the abdominal muscle layer, then the muscle was closed with sutures (4-0 silk, Covidien) (Extended Data Fig. 1b (6)). The WCP (3 × 3 × 0.3 cm) was implanted between the skin and muscle (subcutaneously) ventral and rostral to the muscle incision and the skin was closed with surgical staples (Extended Data Fig. 1b (7–9)). Sham surgeries followed the same protocol and timing without implantation of the device. Both wirelessly powered and battery powered devices were implanted and used throughout the following experiments. **Computed tomography (CT) imaging.** CT images were taken from rats 1 month after implantation of the CLOC system with a Siemens Inveon Micro PET/CT scanner.

Dynamic mechanical analysis. A dynamic mechanical analyser (Q800 DMA; TA Instruments) was used for determining Young's moduli through analysis of measured strain–stress curves. The measurement involved a film tension clamp, a strain rate of 1% per min and a maximum strain of 25%, all performed under ambient conditions. Here, we selected the upper limit strain rate of 1% knowing that the modulus measured at 1% would probably be the highest observed in an awake animal in an experimental setting.

Extraction of mechanical properties of the rat bladder wall. The mechanical properties of the bladder wall can be extracted from measurement of the expansion of the bladder as a function of pressure of saline delivered to its interior. Models of this type of pressure–deformation data approximate the bladder as a shell of spheroidal shape, with initial equatorial radius a_0 and length of the other semi-axis b_0 , and initial thickness t_0 (initial thickness of 0.81 mm). Previous studies have shown that the shape of the bladder (ratio b_0/a_0) has little effect on the pressure–volume relationship^{27,28}. As a result, the spheroidal shape can be approximated as a spherical shell with the same inner volume (the equivalent radius is $(R_0)_{\text{eq}} = \sqrt[3]{a_0^2 b_0}$). After expansion, the equivalent radius is determined as $R_{\text{eq}} = \sqrt[3]{a^2 b}$, where a and b are lengths of the semi-axes of the bladder wall after expansion.

Mechanical analysis gives the nominal biaxial stress in the bladder wall as²⁹

$$\sigma = \frac{P\pi R_{\text{eq}}^2}{2\pi (R_0)_{\text{eq}} t_0} = \frac{PR_{\text{eq}}^2}{2(R_0)_{\text{eq}} t_0} \quad (1)$$

where P is the difference between the inner and outer pressures of the bladder wall. The nominal biaxial strain is given by

$$\varepsilon = \frac{R_{\text{eq}}}{(R_0)_{\text{eq}}} - 1 \quad (2)$$

When the bladder is fully empty ($2a_0 = 3.52$ mm, $2b_0 = 5.83$ mm), the difference between the inner and atmospheric pressures is not zero but is instead 3.2 mm Hg owing to intra-abdominal pressure. In the modelling, the intro-abdominal pressure is subtracted from the actual applied pressure on the bladder wall (Extended Data Fig. 2g, h).

The nominal biaxial stress–strain relationship obtained above is used to fit the Ogden hyperelastic model. Its corresponding uniaxial stress–strain relationship (Fig. 2b) is calculated with the fitted model. FEA shows that the extracted stress–strain relationship from the spherical shell approximation reproduces the expansion of the bladder wall under inner pressure (Extended Data Fig. 2i), which verifies the method described above.

Finite element analysis of bladder expansion. Full three-dimensional FEA was performed using the commercial software ABAQUS (ABAQUS 2016). We used 6,722 shell elements (ABAQUS element type S4R) for modelling of the bladder and 28,800 solid elements (ABAQUS element type C3D8R) for the strain gauge. The mechanical properties of the bladder wall are described by its nominal biaxial stress–strain relation obtained from pressure–expansion data (Extended Data Fig. 2g) as described in the previous section, and then fitted with the Ogden hyperelastic model.

The nonlinear Mooney–Rivlin hyperelastic model was used to characterize the mechanical behaviour of the strain gauge band (including carbon black-doped silicone and undoped neat silicone encapsulation), and material constants in the model were determined by fitting with measured initial modulus (270 kPa and 60 kPa for doped and undoped silicone, respectively). In simulation, the initial length of the strain gauge was taken as 15 mm, which allows conformal contact on an experimentally measured diameter of a specific bladder at contraction state (Extended Data Fig. 2g).

Light penetration through the bladder. To measure light penetration, a rat bladder was removed 7–18 days after CLOC implantation and placed over a light sensor (Thor Labs, power meter PM100D; sensor S121C). A syringe inserted into the neck of the bladder and secured with a suture (4-0 silk) allowed manual inflation with saline. The μ -ILEDs were placed on top of the bladder, directly in contact with the bladder surface, and powered to the same intensity for each experiment. Light power recordings were made with the bladder in the fully inflated and empty states, each with and without μ -ILED illumination to account for ambient light. The bladder was then cut open and a sheet of bladder tissue was placed on the sensor for measurements of light transmission.

Thermal finite element analysis of operation of a μ -ILED. The calculations of the temperature increase with time were obtained by finite element analysis using ABAQUS commercial software (ABAQUS 6.14). The μ -ILED device (4 × 1.1 × 0.7 mm) consists of PDMS (390 μ m thick), PIB (10 μ m thick), epoxy (195 μ m thick), copper (8 μ m thick), PI (12 μ m thick) and stainless-steel layers (25 μ m thick) from top to bottom. The rectangular μ -ILED consists of a layer of SiC and InGaAs with lengths, widths and thicknesses of 270 × 220 × 40 μ m and 270 × 220 × 10 μ m,

respectively. The parameters used in the modelling include conductivity, density, and specific heat^{30–32}. The blood perfusion rate was 0.008 ml/ml/s³³. The computed temperature increases resulted from heat uniformly distributed across the rectangular surface of the μ -ILED, with thermal output power of 70 mW/mm². The modelling results of temperature increment matched experimental findings (Extended Data Fig. 3d, f). In the modelling, a full three-dimensional implicit transient heat transfer model with 2.5 million linear hexahedral DC3D8 elements was established. A schematic illustration of the optoelectronic stimulation and sensing module embedded in the tissue is in Extended Data Fig. 3g. A convergence study has been carried out to ensure the accuracy of the model by increasing the number of elements for steady-state analysis (Extended Data Fig. 3h).

Wireless communication. Experiments used both battery-free and battery-powered devices (wireless powered devices were used in automatic identification of voiding (Extended Data Fig. 9a) and demonstration of prolonged battery-free recording (Extended Data Fig. 9e), all other wireless experiments used the battery-powered design to allow multiple short-term experiments to run concurrently). For the latter, a 90-mAh coin cell battery and a low-dropout regulator replaced the load-coil, impedance matching circuit, and power management circuitry of the former. The remaining circuitry consisted of the radio-embedded microcontroller (nRF51, Nordic Semiconductor) for wireless communication and the bridge circuit to measure the resistance of the strain sensor. A microcontroller embedded with a radiofrequency transceiver and an analogue-to-digital converter sampled measurements and controlled the μ -ILEDs. The resistance of the strain sensor was measured using a bridge circuit and an instrumental amplifier, converted with an internal analogue/digital converter (ADC) in the microcontroller, and transmitted to a user interfacing device every second for further signal processing. A thin layer of copper (12 μ m) and a ferrite shield placed at the base of the WCP module and patterned in the geometry of its constituent components magnetically shielded the system from the incoming RF to minimize parasitic heating and noise of electronic components. A sampling rate of 1 Hz was sufficient to capture the bladder activity (~1 h for bladder to fill and ~30 s to void). Further signal analysis on the iOS application classified overactive bladder activity to determine when to activate the μ -ILEDs (current-controlled at 6.2 mA using a general-purpose input/output on the microcontroller).

Anaesthetized cystometry. Rats were first anaesthetized with urethane (U2500, Sigma) (two IP injections totalling 2 mg/kg, 1 h apart; 0.8 and 1.2 mg/kg; stock solution 150 mg/ml) and then a midline incision was used to expose the bladder dome. After a small incision was made in the dome of the bladder, a flared PE50 catheter (BB31695-PE/3, Scientific Commodities, Inc.) was inserted into the dome of the bladder and secured with a purse string suture³⁴. After the catheter was placed, if a μ -ILED strain gauge was used it was placed around the bladder as described above. The μ -ILED was then connected to a current source (U8031A, Adgilent) and controlled manually. The strain gauge was connected to a digital multimeter device (USB-4065, National Instruments) and data were recorded in LabVIEW (National Instruments) with a developed script to measure changes in resistance. Then the syringe pump was started and the bladder was filled at 0.1 ml/min with room-temperature saline to evoke a regular voiding pattern. Intravesicular pressure was measured using a pressure transducer amplified by a Transbridge 4M amplifier (WPI) and recorded using WINDAQ data acquisition software (DataQ Instruments) at a sampling rate of 5 Hz. After a regular pattern was established, for experiments using the μ -ILED strain gauge, five consecutive contractions (four intercontraction intervals) were recorded for baseline and then the μ -ILED was illuminated for the subsequent five contractions. This was repeated for each animal (total of 2 \times). The first contraction after the light was turned on was not counted for either the baseline or illumination period. For comparison of chronic strain gauge implantation to sham surgery and sham injection to viral injection, 1 h of cystometric voiding was acquired from each animal after a stable pattern developed. Data were analysed using a Matlab (Mathworks) script to determine baseline pressure (BP), threshold pressure (TP), maximum pressure (MP) and intercontraction interval (ICI) (terminology as described³⁵). Compliance was calculated as (flow rate \times (time_{BP} – time_{TP}))/(TP – BP). Rats that did not develop a regular cystometric pattern were excluded from analysis.

Novel environment exploratory behaviour. To test whether rats implanted with the CLOC device had altered exploratory behaviour, we tracked movement in a novel environment (42 \times 42 \times 30 cm, length \times width \times height) 7 days after CLOC device implantation. Rat movement was tracked using a VersaMax Animal Activity Monitoring System (AccuScan Instruments, Inc., Columbus, OH) and distance travelled during the 30-min test period was calculated.

Gait analysis. Gait analysis was performed using the automated gait analysis hardware (Catwalk XT 10.5, Noldus). Gait analysis was completed with the standard rat calibration (camera gain, green light intensity, run duration, run maximum variation). All animals were acclimatized to the Catwalk system twice for 15 min, 1 day before testing. Rats were tested 7 days after CLOC device implantation. Four compliant runs were required for each rat and parameters were averaged.

Mast cell degranulation. Seven days after viral injection into the bladder (or sham injection), rats were deeply anaesthetized with an IP injection of ketamine cocktail (ketamine (100 mg/ml), xylazine (20 mg/ml) and acepromazine (10 mg/ml)) and then transcardially perfused with 1 \times phosphate-buffered saline (PBS; pH 7.2) followed by cold 4% paraformaldehyde (PFA). Bladders were equilibrated in 30% sucrose, frozen in OCT (Tissue Tek), and 20- μ m cross sections were thaw-mounted directly onto SuperFrost plus slides (Fisher Scientific) using a cryostat. Slides were blinded and stained with acidified toluidine blue solution to visualize mast cells (working solution of 0.002 g/ml toluidine blue O (Sigma) in 1% sodium chloride, pH 2.0–2.5). Total numbers of mast cells were counted and added across three cross sections—one from each third of the bladder (base, middle, and dome). This was performed in duplicate and averaged. Cells were considered degranulated if there was an extensive dispersion of more than 15 extruded vesicles localized near the cell.

Viral transduction of bladder afferents. HSV-hCMV-eYFP and HSV-hCMV-Arch3.0-eYFP viral preparations were obtained from Massachusetts Institute of Technology viral core (R. Neve, MIT McGovern Viral Core Facility). The original Arch3.0 (Arch) construct was cloned by the Deisseroth Laboratory. Viruses were obtained at a titre of $\sim 3.5 \times 10^9$ infectious units per ml and diluted to 2.1×10^9 immediately before injection. Viral injections into the bladder were performed to drive transgenic expression of eYFP or Arch selectively in peripheral bladder-innervating neurons. After achieving and confirming full anaesthesia using 3% isoflurane, a laparotomy was performed with a small transverse incision in the muscle and skin to expose the bladder. The bladder, if full, was manually expressed to remove the majority of the urine. Then, using a 35 ga Nanofil needle (WPI) and syringe, four injections of 5 μ l of either HSV-CMV-eYFP or HSV-CMV-Arch-eYFP ($\sim 2.1 \times 10^9$ infectious units total per injection) were made in to the bladder wall, equal distances apart around the base of the bladder. The needle was left in position for 1 min following each injection and then slowly removed to prevent leakage of the virus. Additionally, after all injections were completed, we waited an additional 5 min before closing to allow further undisturbed absorption. Next the muscle was closed with 5-0 nylon sutures and the skin was closed with surgical staples. Optogenetic experiments were then performed 6–8 days after injection.

Immunohistochemistry (bladder whole mount). Bladders were removed after transcardial perfusion with 1 \times PBS, then cut from the base to the dome and pinned flat in a Sylgard dish. Bladders were covered with 4% PFA and fixed for 4 h to overnight. The urothelial/interstitial layers were then carefully dissected away from the smooth muscle layer. The bladder was washed again in 1 \times PBS for 3 \times 5 min and incubated in blocking solution (5% normal goat serum/0.3% Triton-X/1 \times PBS) for 2 h at room temperature. The primary antibodies (1:1,000 chicken anti-GFP (Aves GFP-1020) and 1:1,000 rabbit anti- β -tubulin (BioLegend 802001)) were diluted in blocking buffer and incubated on the sections for 5–6 days at 4 $^{\circ}$ C with gentle agitation. Bladders were washed 5 \times for 15 min each with 1 \times PBS and then incubated with secondary antibodies in blocking solution for 2 h at room temperature (1:1,000 goat anti-rabbit IgG Alexa Fluor 555 (Thermo Fischer A21422), 1:1,000 goat anti-chicken IgG Alexa Fluor 488 (Thermo Fischer A11039)). Samples then were washed 5 \times for 15 min with 1 \times PBS, floated on to slides (Fisher Scientific), and coverslipped using Vector Shield Hard Set mounting medium. Whole-mount samples were then imaged on a scanning confocal microscope (Leica). All whole mounts shown are from the urothelial and interstitial layers.

Immunohistochemistry (DRG and bladder H&E staining). DRGs were sectioned and stained as previously described³⁶. In brief, 6–8 days after HSV viral vector injection, rats were perfused with PBS and 4% PFA as described above. L6–S1 DRGs were extracted, post-fixed in 4% PFA overnight, and then transferred to 30% sucrose for 24 h. DRGs were then frozen in Tissue Tek Optimal Cutting Temperature (OCT) medium (Sakura Finetek), sectioned on a cryostat (Leica) at a thickness of 15 μ m, and placed directly onto slides. Slides were post-fixed with 4% PFA for 5 min, then thoroughly washed 3 \times for 5–10 min. Slides were incubated with blocking buffer (1 \times PBS, 5% goat serum, 0.3% Triton-X) for 1 h, followed by primary antibodies (1:1,000 chicken anti-GFP (Aves GFP-1020) and 1:1,000 rabbit anti- β -tubulin (BioLegend 802001)) overnight at 4 $^{\circ}$ C. Slides were subsequently washed 3 \times with PBS and then incubated with the appropriate secondary antibodies (1:1,000 goat anti-rabbit IgG Alexa Fluor 555 (Thermo Fischer A21422), 1:1,000 goat anti-chicken IgG Alexa Fluor 488 (Thermo Fischer A11039)) for 45 min at room temperature. Slides were finally washed 4 \times for 10 min in PBS and coverslipped with Prolong Gold mounting medium (P36934, Life Technologies). Slides were imaged on a confocal microscope and images processed using NIH Image J software. For haematoxylin and eosin (H&E) staining, the bladder was removed and then only the segment of bladder that contacted the band (or where the band would be in sham animals) was sectioned onto slides, which were post-fixed in ethanol and then stained with a standard H&E protocol³⁷. For quantification of bladder thickness, two images of bladder were taken and the distance between

lumen and the outer smooth muscle layer was measured in three locations and averaged by a blinded experimenter.

Rat DRG culture. Rats were injected with DiI (ThermoFisher, 10 μ l) into the bladder wall 7–10 days before DRG culture. DRG cultures were performed as previously described in mice³⁶. In brief, rats were anaesthetized with ketamine cocktail and then quickly perfused with PBS. DRGs were removed and dissociated enzymatically with papain (Worthington) and collagenase type 2 (Sigma), and mechanically with trituration. Final solutions were filtered (40 μ m, Fisher) and cultured with DRG medium (5% fetal bovine serum (Gibco) and 1% penicillin/streptomycin (Corning) in Neurobasal A medium 1 \times (Gibco) plus Glutamax (Life Technologies) and B27 (Gibco).

Human DRG culture. Human DRGs were extracted, dissected and cultured as described previously³⁸. In brief, in collaboration with Mid-America Transplant Services, L1–L5 DRG were extracted from a tissue/organ donor less than 2 h after aortic cross clamp. The donor was a 25-year-old black female with a BMI of 21 and cause of death due to head trauma from a motor vehicle accident. DRGs were placed in an *N*-methyl-D-glucamine (NMDG) solution for transport to the laboratory, fine dissection, and mincing. Pieces were dissociated enzymatically with papain (Worthington) and collagenase type 2 (Sigma), and mechanically with trituration. Final solutions were filtered (100 μ m, Fisher) and cultured with DRG medium (5% fetal bovine serum (Gibco) and 1% penicillin/streptomycin (Corning) in Neurobasal A medium 1 \times (Gibco) plus Glutamax (Life Technologies) and B27 (Gibco).

Viral transduction of DRG cultures. Rat and human DRG neurons were transduced with HSV carrying a transgene for the inhibitory proton pump Arch (HSV-hCMV-Arch3.0-eYFP). Virus was added at a final concentration of 1.75×10^8 infectious units per ml either immediately after culturing (rat) or after 8–9 days in vitro (human). Neurons were used for electrophysiological recording from 24–48 h post-transduction.

Whole-cell patch-clamp electrophysiology. Electrophysiological recordings from cultured rat and human DRG neurons were carried out in an external solution consisting of (in mM): 145 NaCl, 3 KCl, 2 CaCl₂, 1.2 MgCl₂, 7 glucose and 10 HEPES, pH 7.3 with NaOH and ~305 mOsm. Patch pipettes were pulled from borosilicate glass electrodes, and had resistance values of 2–3 M Ω (human) and 3–4 M Ω (rat) when filled with (in mM): 120 potassium gluconate, 5 NaCl, 2 MgCl₂, 0.1 CaCl₂, 10 HEPES, 1.1 EGTA, 4 Na₂ATP, 0.4 Na₂GTP, 15 sodium phosphocreatine, pH 7.3 with KOH, 291 mOsm. Fluorescence imaging and photostimulation were performed using custom-built LEDs (M470L2 and M530L3, Thorlabs) coupled to the epi-fluorescence port of an upright microscope (BX-51, Olympus). LEDs were positioned for Köhler illumination, and light intensity was calibrated using a photodiode (S120C, Thorlabs) and power meter (PM100D, Thorlabs). Recordings were made using Patchmaster software controlling a HEKA EPC10 amplifier, low-pass filtered (Bessel 10 kHz), and digitized at 20 kHz. Action potential thresholds were determined from a holding potential of -60 mV with a series of 1-s depolarizing current injections in increments of 10 pA (rat) or 100 pA (human). Action potential frequencies were elicited in response to suprathreshold stimuli at 1–4 times rheobase, both before and during constant illumination with 530 nm green LED light at 3.3 or 10 mW/mm² (M530L3, Thorlabs). Series resistance was kept below 10 M Ω in all recordings. Data were analysed offline using custom-written macros and the Neuromatic plug-in (<http://www.neuromatic.thinkrandom.com>) in Igor Pro (WaveMetrics; Portland, OR).

Bladder inflammation model. Cyclophosphamide (C0768, Sigma) is metabolized to acrolein, which is excreted by the kidneys into the bladder where it causes bladder-specific inflammation and increases voiding frequency³⁹. A single dose of 75 mg/kg cyclophosphamide (CYP, IP) was used for the open-loop/user-controlled experiments (Fig. 3e, f). One injection of 150 mg/kg CYP IP was used for the closed-loop experiments. CYP was used because it can cause increased voiding frequency with a single IP injection, and other methods are more invasive (intravesical infusion) or take a long time to develop (stress-induced increases in voiding)⁴⁰.

Assessment of visceral motor reflex. The visceral motor reflex (VMR) was measured by recording abdominal electromyographs (EMG) in response to bladder distension as previously described^{36,41}. In brief, rats previously injected with either saline (vehicle) or 150 mg/kg CYP 16–24 h before VMR recordings were anaesthetized with isoflurane (2%). They were then catheterized with a 24-gauge angiocatheter and electrodes were placed into the external oblique muscle, to measure EMG responses. Then the anaesthetic concentration was slowly tapered down to 1.25%. After stabilization at the lower anaesthetic concentration, phasic urinary bladder distensions (20–70 mmHg) were delivered through the angiocatheter and corresponding EMG responses recorded. For analyses, baseline EMG was subtracted from the distension response and the remaining EMG response was rectified and intergraded to collect the distension evoked EMG. All distensions were completed in triplicate and averaged for each individual animal.

Open-loop/user-controlled μ -ILED experiments. Rats were injected with either HSV-CMV-eYFP or HSV-CMV-Arch-eYFP at day 0 and implanted with the

CLOC system on day 3. On day 5 rats were acclimated in modified metabolic rat cages above computerized balances (Columbus Instruments) for at least two 45–60-min sessions at least 1 h apart. On day 6 they were put in the metabolic cage or kept in the home cage in the same room and the μ -ILEDs were turned on or left off for 3 h, depending on the treatment group. Some experiments were performed in metabolic cages to confirm voiding events to understand the relationship between strain gauge resistance and voids (training set). On day 7 rats were injected with CYP (75 mg/kg, IP) at the same time of day as the baseline test and put in the metabolic cage or left in the home cage. μ -ILEDs were turned on (or not) and strain and metabolic data were recorded for 3 h. All void analysis was done posthoc (Microsoft Excel). If an animal did not void within the 3 h, a value of 180 min was assigned. Voids were identified by the methods outlined below.

Void identification signal analysis and verification. To identify voiding events, raw strain gauge data were analysed using multiple-step signal processing. Standard deviation (s.d.) was calculated for each animal to account for device-to-device variability in noise and degree of change during filling and emptying events. The s.d. was taken from ~1 h of raw data without a void. Raw data voids were identified by the following four steps: 1) take a moving 60-point (1 min) average; 2) down-sample to 4 points per second (from 1 point per second); 3) calculate the derivative of the down-sampled data; 4) if three consecutive derivative values are less than $3 \times$ the negative s.d., this is counted as a preliminary void. There were two conditions when preliminary voids calculated in this way were rejected: when there was a void in the previous 5 min and if there was a significant positive derivative value, indicating animal movement, preceding the void. A significant positive derivative value was calculated by averaging only the positive derivative values from the previous 10 points (2.5 min). If this value was higher than 40% of the s.d. (with a minimum value of 7) then the preliminary void was eliminated and counted as noise.

User interface and voiding identification. Software developed using XCode and operating on a tablet computer (iPad mini 2 and iPad Air 2, Apple) served to capture and compile strain gauge data. The iOS application 1) logs strain gauge data for post-data analysis; 2) defines μ -ILED protocols for optogenetic activation; and 3) sets calibration parameters for closed-loop experiments. Also, the UI displays 30-min graphical plots of raw, filtered, and derivative SG data for troubleshooting. iOS code is available at https://github.com/noh21/bladder_cloc.

Operationally, the application first logs strain gauge data (sampled at 1 Hz) in a text file format in the iOS device after establishing a Bluetooth connection to the implanted WCP device. Comparing strain gauge data with metabolic cage data sets the foundation the signal processing requires for closed-loop function. Second, the manual μ -ILED switch and textboxes located at the top of the GUI enable open-loop optogenetic experiments. Turning on the 'Manual LED' switch activates a μ -ILED protocol that follows an on/off timing pattern defined in the text boxes. Lastly, the closed-loop experimental function engages after a series of open-loop experiments. The 'Automated Closed-Loop' switch turns on closed-loop functionality with calibration parameters defined in the textboxes. The parameters 'Device STD, Noise Threshold, and Voiding Interval' are calibration metrics determined via data collected before the closed-loop experiments to account for variances among devices and rats. A series of signal processing steps determines whether a voiding has occurred (described above). If three voiding events occur within a preset interval, the μ -ILED protocol is activated.

Closed-loop experiments. Rats were injected with HSV-eYFP or HSV-Arch-eYFP and implanted with the CLOC system 6 days before the experiment. On the 6th post-operative day (POD), strain gauge data were collected to calculate the s.d. in order to calculate the threshold for voiding, for each individual animal. On the morning of POD 7 (~08:00) the closed-loop program (Fig. 4c) was activated while the rat was in its home cage. At ~12:00, the closed-loop program was turned off and the animals were injected with 150 mg/kg CYP. The program was turned off to prevent accidental activation due to handling of the animal. Fifteen minutes after the injection of CYP, the closed-loop program was turned on. Data were analysed as described above.

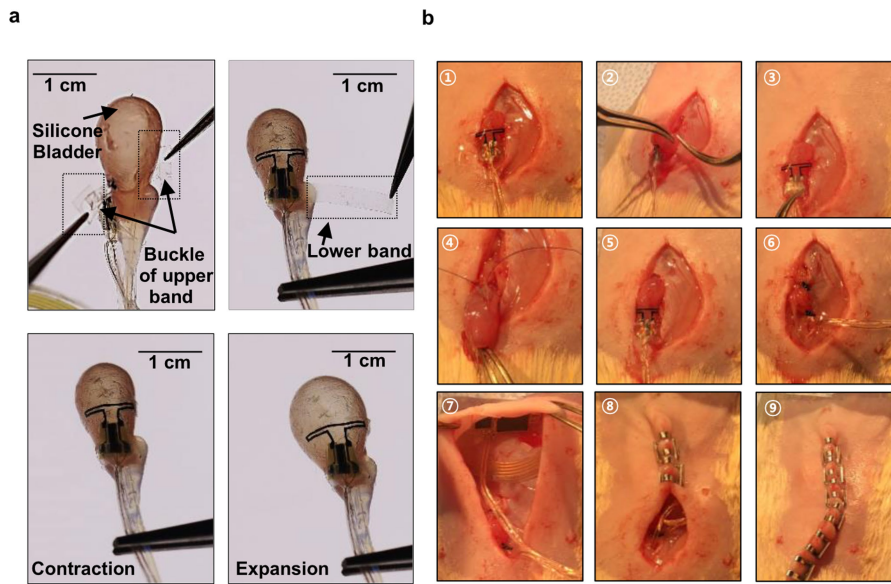
Statistics and reproducibility. All experiments were performed in female rats (200–300 g) that were randomly assigned to control or experimental groups for virus injection, device implantation or culture. Sample sizes were determined from preliminary experiments using the software G*power for the appropriate type of statistical comparison. In the open- and closed-loop experiments, data were excluded from animals in which the closed-loop bladder device malfunctioned or was damaged. All data were collected in a non-biased manner and experimenters were blinded to treatment for final analysis. Unpaired *t*-tests and Mann–Whitney tests, as well as one-way and two-way ANOVAs, were performed as appropriate. *P* values < 0.05 were considered statistically significant. All results are represented as mean \pm s.e.m. Experiments were repeated as follows: Fig. 2e three times; Fig. 3a more than ten times; Fig. 3b four times; and Fig. 4b three times, all in biologically independent animals with similar results. See Supplementary Table 1 for all statistical details.

Reporting summary. Further information on research design is available in the Nature Research Reporting Summary linked to this paper.

Data availability

The data that support the findings of this study are either provided in the source data or are available from the corresponding authors upon reasonable request. iOS code is available at https://github.com/noh21/bladder_cloc.

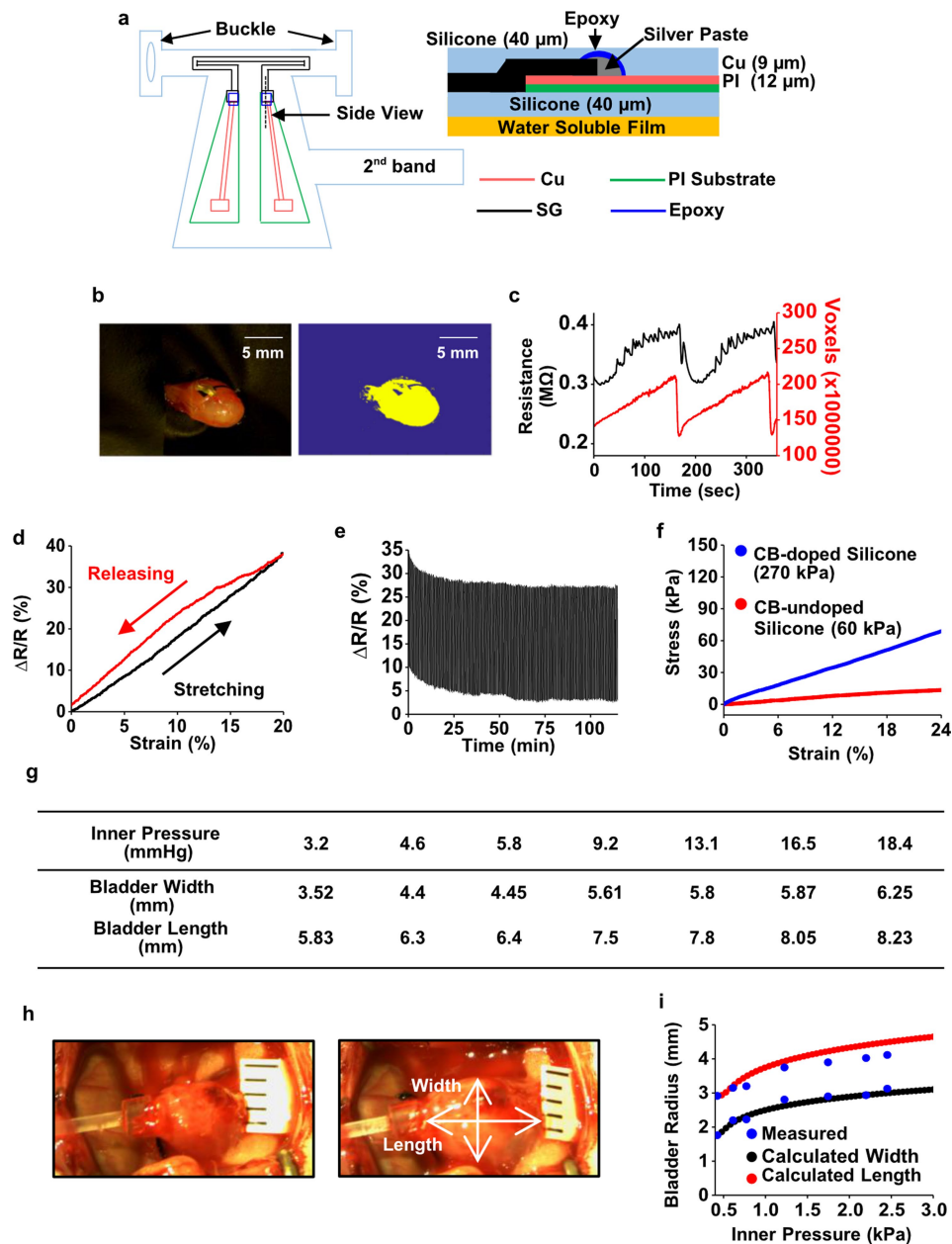
25. Gutierrez, C. A. & Meng, E. Low-cost carbon thick-film strain sensors for implantable applications. *J. Micromech. Microeng.* **20**, 095028 (2010).
26. Lu, N., Lu, C., Yang, S. & Rogers, J. Highly sensitive skin-mountable strain gauges based entirely on elastomers. *Adv. Funct. Mater.* **22**, 4044–4050 (2012).
27. Damaser, M. S. & Lehman, S. L. Does it matter, the shape of the bladder? *NeuroUrol. Urodyn.* **12**, 277–280 (1993).
28. Korkmaz, I. & Rogg, B. A simple fluid-mechanical model for the prediction of the stress-strain relation of the male urinary bladder. *J. Biomech.* **40**, 663–668 (2007).
29. Kelly, P. Mechanics Lecture Notes: An introduction to Solid Mechanics. <http://homepages.engineering.auckland.ac.nz/~pkel015/SolidMechanicsBooks/index.html>, 185–194 (2018).
30. Ren, Y., Qi, H., Chen, Q. & Ruan, L. Thermal dosage investigation for optimal temperature distribution in gold nanoparticle enhanced photothermal therapy. *Int. J. Heat Mass Transfer* **106**, 212–221 (2017).
31. Samineni, V. K. et al. Fully implantable, battery-free wireless optoelectronic devices for spinal optogenetics. *Pain* **158**, 2108–2116 (2017).
32. Bhattacharya, A. & Mahajan, R. L. Temperature dependence of thermal conductivity of biological tissues. *Physiol. Meas.* **24**, 769–783 (2003).
33. Liu, J., Zhu, L. & Xu, L. X. Studies on the three-dimensional temperature transients in the canine prostate during transurethral microwave thermal therapy. *J. Biomech. Eng.* **122**, 372–379 (2000).
34. Uvin, P. et al. The use of cystometry in small rodents: a study of bladder chemosensation. *J. Vis. Exp.* **66**, e3869 (2012).
35. Andersson, K. E., Soler, R. & Füllhase, C. Rodent models for urodynamic investigation. *NeuroUrol. Urodyn.* **30**, 636–646 (2011).
36. Samineni, V. K. et al. Optogenetic silencing of nociceptive primary afferents reduces evoked and ongoing bladder pain. *Sci. Rep.* **7**, 15865 (2017).
37. Park, S. I. et al. Soft, stretchable, fully implantable miniaturized optoelectronic systems for wireless optogenetics. *Nat. Biotechnol.* **33**, 1280–1286 (2015).
38. Valtcheva, M. V. et al. Surgical extraction of human dorsal root ganglia from organ donors and preparation of primary sensory neuron cultures. *Nat. Protocols* **11**, 1877–1888 (2016).
39. Lai, H. et al. Animal models of urologic chronic pelvic pain syndromes: findings from the multidisciplinary approach to the study of chronic pelvic pain research network. *Urology* **85**, 1454–1465 (2015).
40. Parsons, B. A. & Drake, M. J. in *Urinary Tract. Handbook of Experimental Pharmacology* (eds Andersson, K. E. & Michel, M.) 15–43 (Springer, Berlin, 2011).
41. Crock, L. W. et al. Central amygdala metabotropic glutamate receptor 5 in the modulation of visceral pain. *J. Neurosci.* **32**, 14217–14226 (2012).



Extended Data Fig. 1 | Demonstration of optoelectronic stimulation and sensing module features and implantation of the whole CLOC system. **a**, Demonstration of strain gauge placement on a mimic bladder illustrating how the two silicone bands wrap around the bladder and how stretch is exerted on the strain gauge as the bladder expands.

b, Detailed surgical procedure for implantation of the wireless closed-loop optogenetics-based system for peripheral neuromodulation. The strain gauge is placed on the bladder (1), and using curved forceps the lower band is pulled under the bladder and wrapped back on top

of the optoelectronic stimulation and sensing module (2). Kwik-Sil is then applied to secure the lower band to the top of the optoelectronic stimulation and sensing module (3). The upper band is then wrapped around the largest part of the bladder dome and the buckle secured. Then a small suture is placed through the buckle into the bladder smooth muscle layer to secure the upper band to the bladder (4). The bladder is then placed back into the abdominal cavity (5) and muscle layers are closed with sutures (6). The WCP is inserted between the skin and the muscle layer (7) and the skin is closed with surgical staples (8, 9).



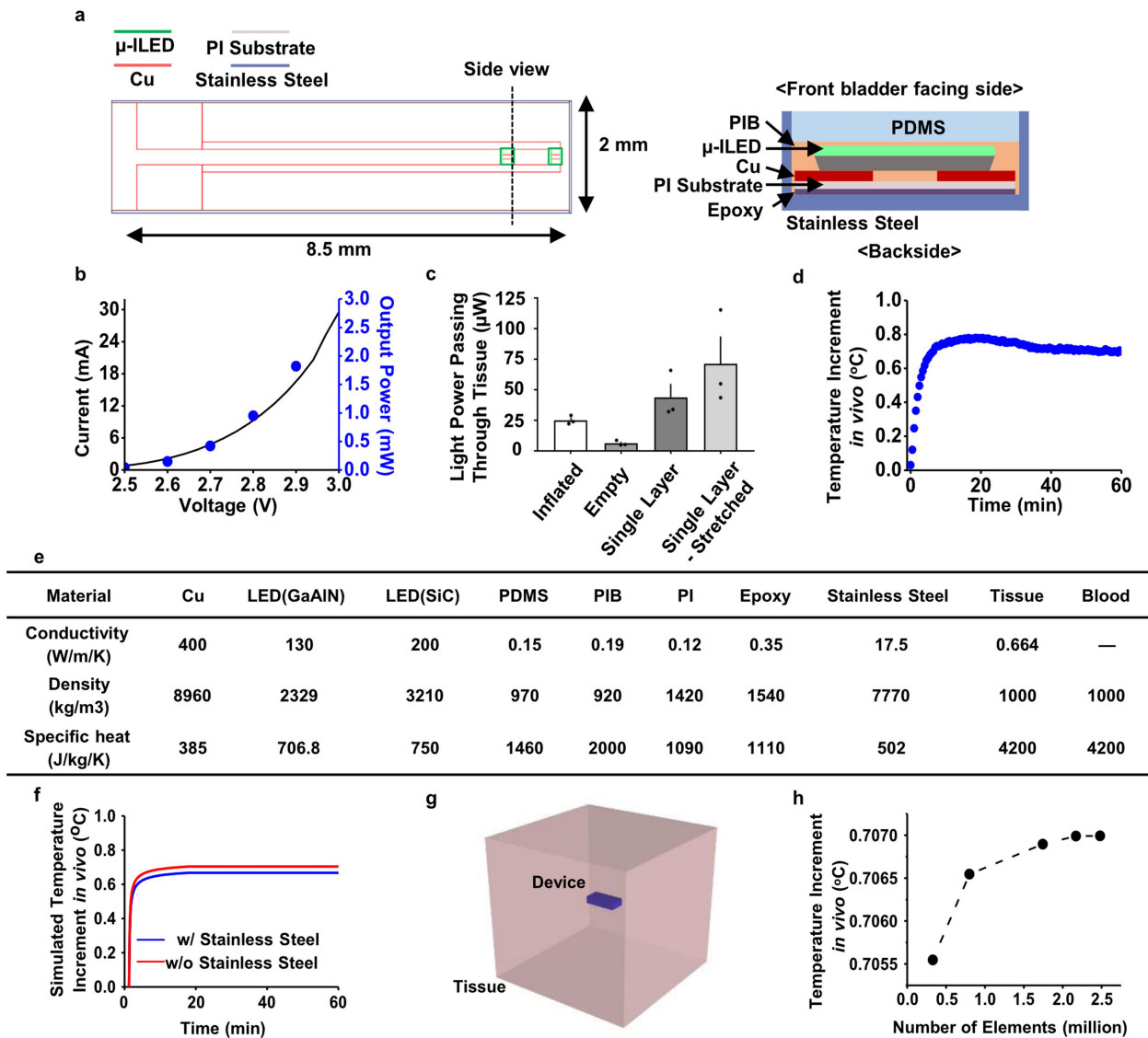
Extended Data Fig. 2 | Computational and experimental studies of the bladder strain gauge and material properties of rat bladder.

a, Left, schematic illustration of a strain gauge, part of the optoelectronic stimulation and sensing module. Right, cross-sectional side view of the device components at the level of the dashed line shown on the left.

b, Image of a rat bladder (left) and digitally manipulated version (right) to allow measurements of the volumetric changes in size during cystometry.

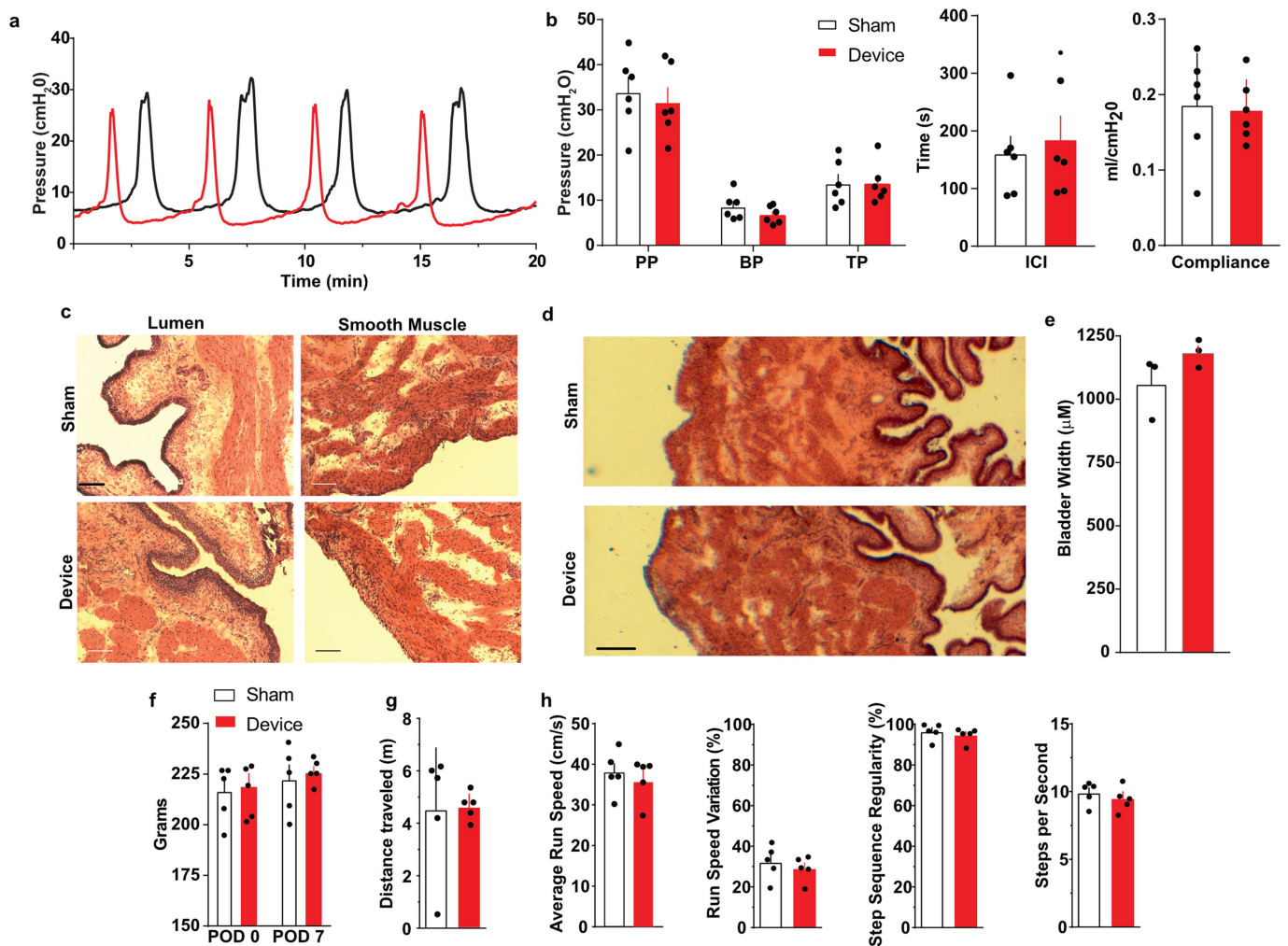
c, Graph of changes in bladder size (red) and changes in strain gauge resistance (black). **d**, Fractional change in resistance of the strain gauge

as a function of uniaxial tensile strain. **e**, Fractional change in resistance under 1,000 cycles of stretching to a maximum strain of 20%. **f**, Uniaxial strain–stress curve of carbon black (CB)–silicone composite and undoped neat silicone. **g**, Length and width of the bladder measured using Vernier calipers at different inner pressures: 3.2 mm Hg (left) and 18.4 mm Hg (right) (ruler, 1 mm). **i**, Simulation results for the width and length of the bladder based on measured values of the inner pressure and the initial length and width.



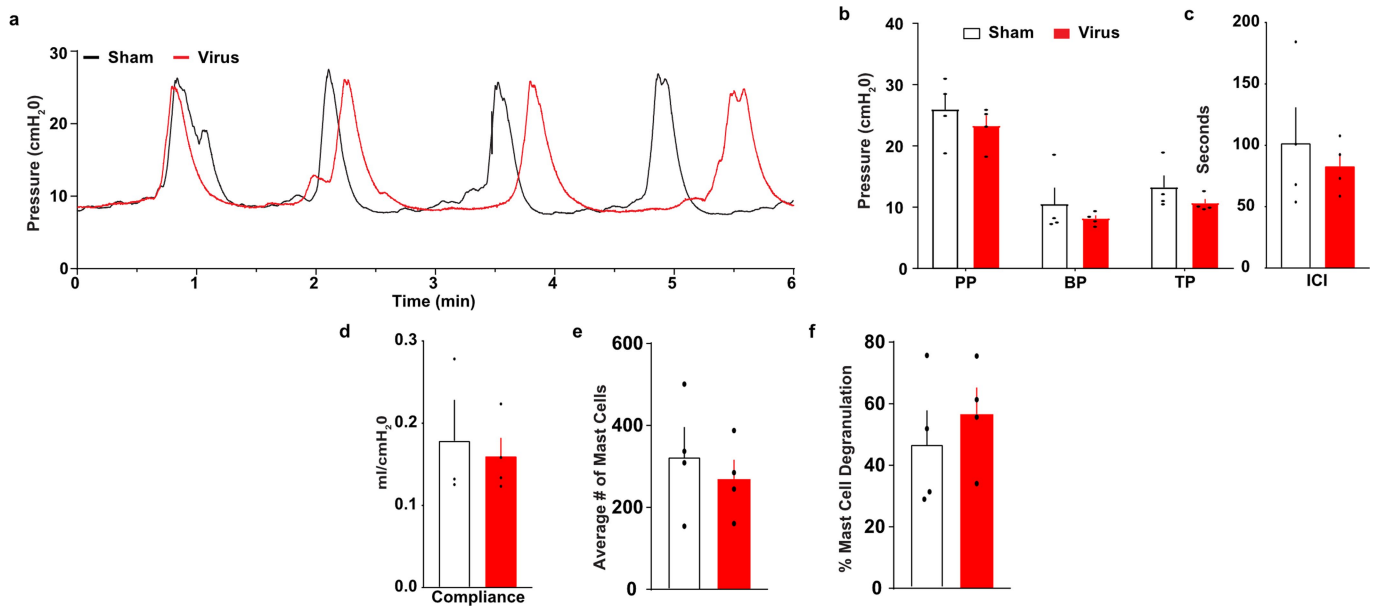
Extended Data Fig. 3 | Optical and thermal characteristics of the μ -ILEDs. **a**, Schematic illustration of the μ -ILED portion of the optoelectronic stimulation and sensing module. **b**, Electrical and optical characteristics of a pair of μ -ILEDs. **c**, Measured power associated with penetration of light from a μ -ILED through the whole rat bladder (both layers) at fully inflated and empty states; additional calculations were performed on single bladder layer relaxed and manually stretched. Performed in three biologically independent samples, mean \pm s.e.m.

d, Results from in vivo testing of the temperature associated with operation of the μ -ILEDs for an hour. **e**, The material properties of the model. **f**, Simulated results for the temperature associated with operation of the μ -ILEDs with and without the stainless-steel substrate. **g**, Schematic illustration of optoelectronic stimulation and sensing module embedded in tissue with dimensions of $30 \times 30 \times 30 \text{ mm}^3$ in the FEA model. **h**, The effect of number of elements in the FEA model on the temperature increments in vivo with power of 70 mW for steady-state analysis.



Extended Data Fig. 5 | Effect of optoelectronic stimulation and sensing module implantation or sham surgery on bladder cystometric properties, histology and animal health. **a**, Representative traces of anaesthetized constant infusion (0.1 ml min^{-1}) cystometric voiding from rats that had undergone sham surgery or CLOC device implantation. **b**, Quantification of peak pressure (PP), base pressure (BP), and threshold pressure (TP) indicates no significant differences between sham-operated and device-implanted groups. The data indicate no significant differences in intercontraction interval (ICI) or bladder compliance ($\Delta\text{volume}/\Delta\text{pressure}$) between sham-operated and device-implanted animals ($n = 6$ rats per group). **c**, Representative H&E staining of bladder tissue in direct contact with the strain gauge and the full CLOC device in implanted rats, and the same tissue from sham-surgery rats (no overt histological differences were observed in these tissues ($n = 3$ for each

group) in biologically independent samples with similar results). Scale bar, $100 \mu\text{m}$. **d**, **e**, Examples (scale bar, $250 \mu\text{m}$; **d**) and quantification (**e**) of bladder thickness, comparing device-implanted and sham-operated animals ($n = 3$ biologically independent tissues in each group). **f**, Sham-operated and device-implanted animals gained similar amounts of weight by post-operative day (POD) 7 ($n = 5$ biologically independent animals in each group). **g**, Animals from both groups ran similar distances in a novel arena ($42 \times 42 \times 30 \text{ cm}$) ($n = 5$ biologically independent animals in each group). **h**, Implantation of the CLOC system did not significantly affect measurements of gait, including average run speed, run speed variation, step sequence regularity and steps per second (cadence) ($n = 5$ rats per group). All data represented as mean \pm s.e.m analysed by two-way ANOVA with Sidak's multiple comparisons test, unpaired t -test or Mann-Whitney test (details in Supplementary Table 1).

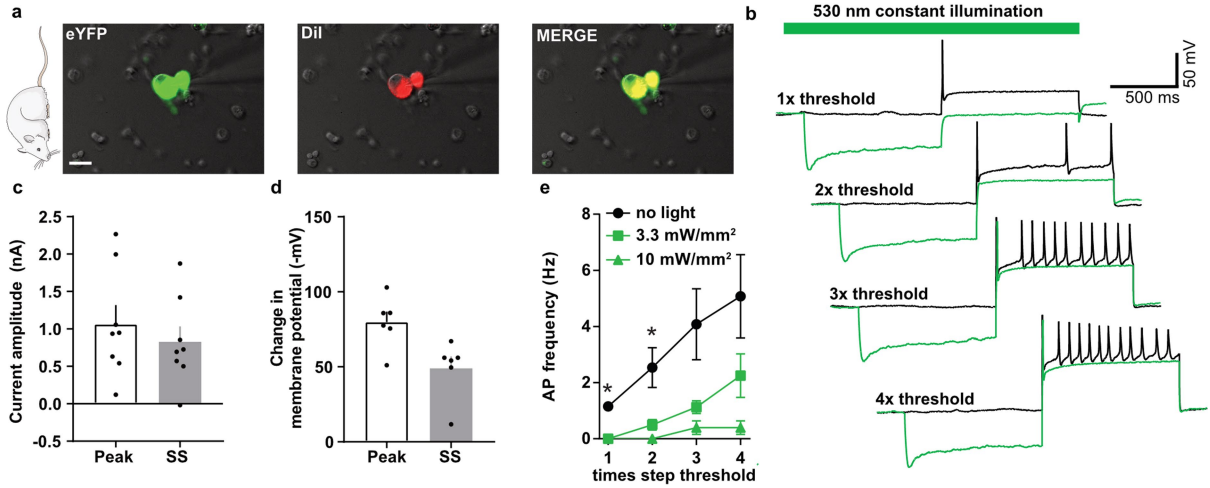


Extended Data Fig. 6 | Bladder cystometric properties and markers of inflammation are not significantly altered by injection of HSV-eYFP compared to sham surgery. **a**, Representative traces of constant infusion (0.1 ml min⁻¹) anaesthetized (urethane) cystometric voiding from sham-injected and virus-injected (HSV-CMV-eYFP) rats.

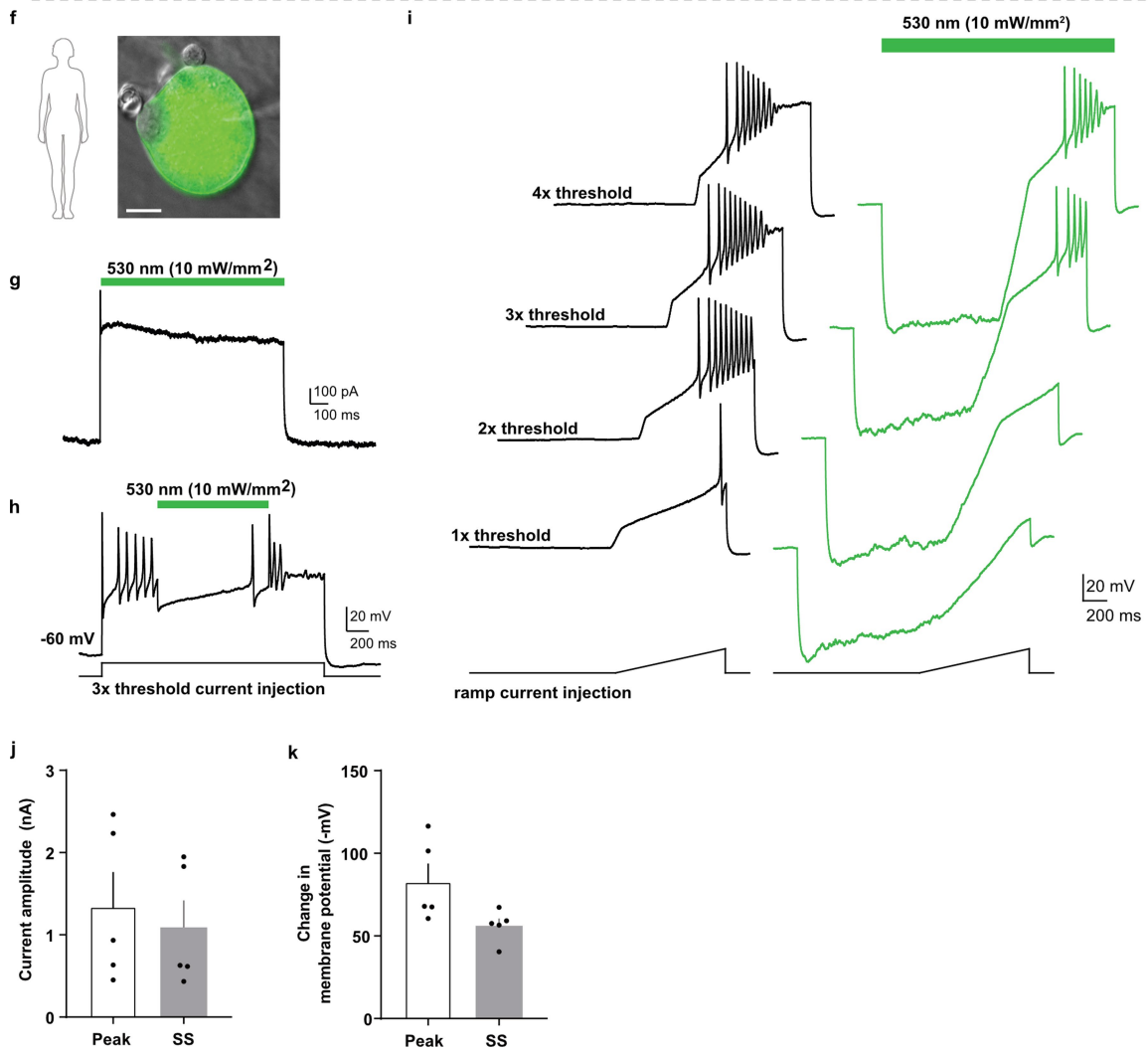
b, Quantification of peak pressure (PP), base pressure (BP), and threshold pressure (TP) indicated no significant differences between sham-injected and virus-injected groups. **c**, **d**, There were no significant differences

in intercontraction interval (ICI) (**c**) or bladder compliance (Δ volume/ Δ pressure) (**d**) between sham-injected and virus-injected rats. **e**, **f**, No significant difference was observed in average number of mast cells (**e**) or degree of degranulation (**f**), indicating that no overt inflammatory response is detected in bladders injected with HSV-eYFP versus sham surgery 7 days after injection. $n = 4$ rats per group; all data mean \pm s.e.m; analysed by two-way ANOVA with Sidak's multiple comparisons test or unpaired t -test (details in Supplementary Table 1).

Cultured Rat Dorsal Root Ganglion



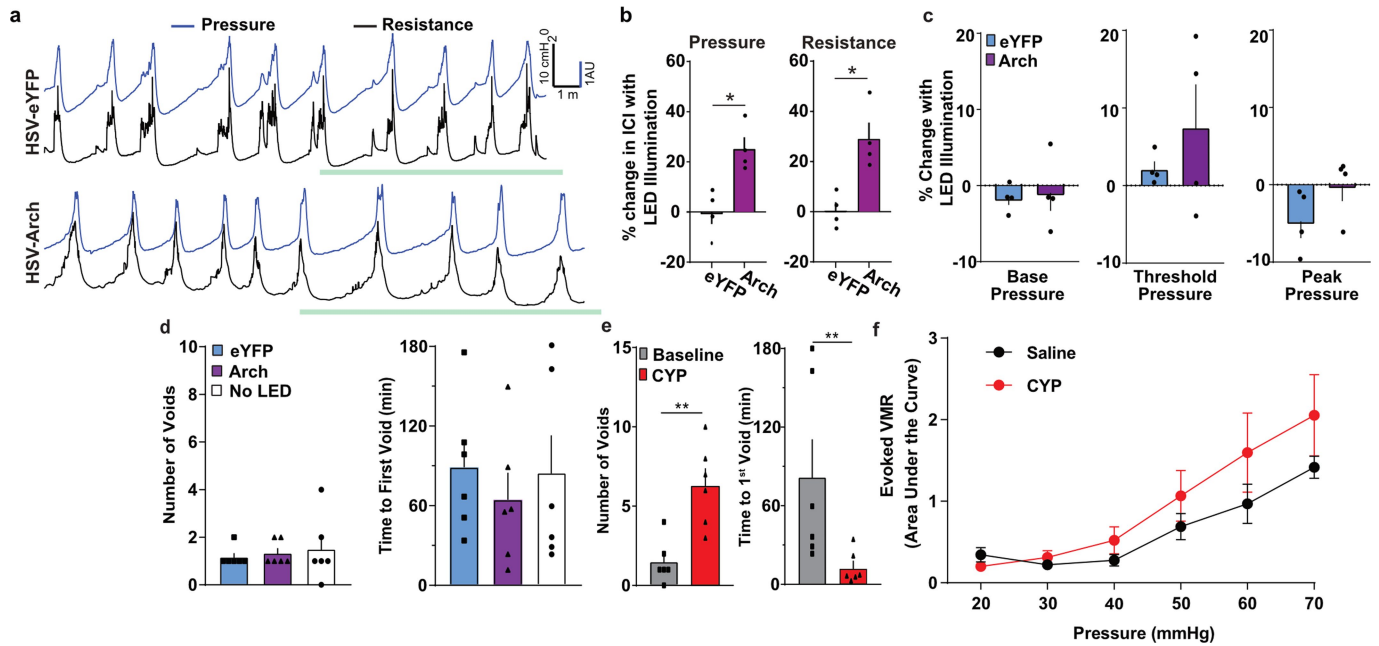
Cultured Human Dorsal Root Ganglion



Extended Data Fig. 7 | See next page for caption.

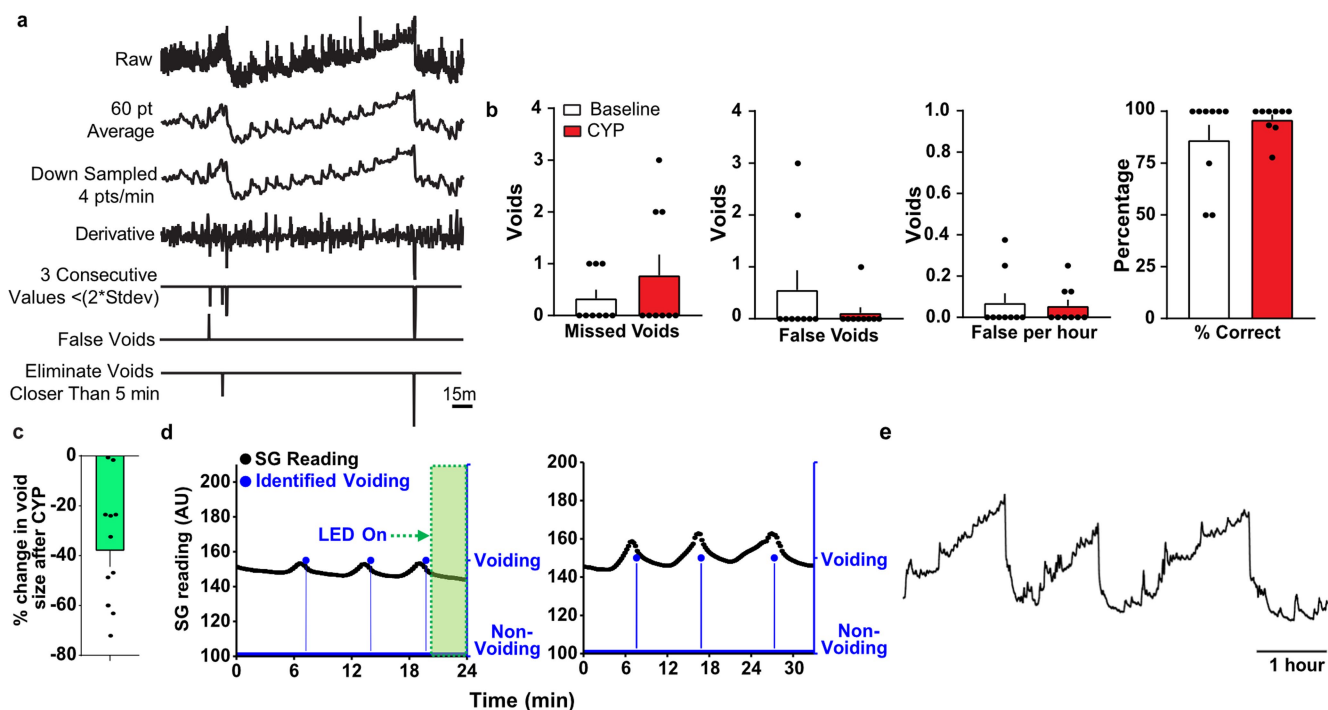
Extended Data Fig. 7 | Activation of Arch in cultured bladder-projecting rat DRG neurons and human DRGs reduces neuronal excitability. **a**, Example of a neuron transduced with HSV-Arch-eYFP (green) and identified as a neuron that projects to the bladder by labelling with DiI (red) following DiI injection into the bladder wall (7 days before). Scale bar, 20 μm ; similar to results obtained from three independent experiments. **b**, Representative traces of DRG neuron firing properties in response to step current injection at 1–4 \times threshold with (green) and without (black) green light illumination (530 nm) (similar to results obtained from three independent cultures). **c**, **d**, Quantification of Arch-induced current amplitude in voltage clamp (**c**) and membrane hyperpolarization in current clamp (**d**) at peak and steady states. **e**, Quantification of action potential (AP) frequency with and without illumination, demonstrating light-dependent inhibition of AP firing. No light $n = 13$; 3.3 mW mm⁻² $n = 8$; 10 mW mm⁻² $n = 5$ different cells, from three biologically independent cultures; all data mean \pm s.e.m.; one-way ANOVA with Dunnett's multiple comparisons test; * $P < 0.05$ (further

statistical details can be found in Supplementary Table 1). **f**, Example of a patched human DRG neuron transduced with HSV-Arch-eYFP. Scale bar, 20 μm . **g**, Example voltage clamp trace demonstrating the photocurrent elicited by green light (530 nm). **h**, Representative current clamp trace demonstrating the ability of Arch to inhibit neuronal firing in response to 3 \times threshold current injection. **i**, Current clamp traces with (green) and without (black) activation of Arch, showing a reduction in action potential firing in response to 1–4 \times threshold ramp currents. **j**, **k**, Quantification of light-induced current in voltage clamp (**j**) and hyperpolarization in current clamp (**k**) at peak and steady state (SS) in Arch-expressing human DRG neurons. $n = 5$ neurons; all data mean \pm s.e.m. **f–h**, Repeated in 5 different cells from one culture, with similar biological results. Cartoon images in **a** and **f** are from Servier Medical Art by Servier (<https://smart.servier.com/>), and are covered by a Creative Commons 3.0 attribution license (<https://creativecommons.org/licenses/by/3.0/>). No changes were made to the original artwork.



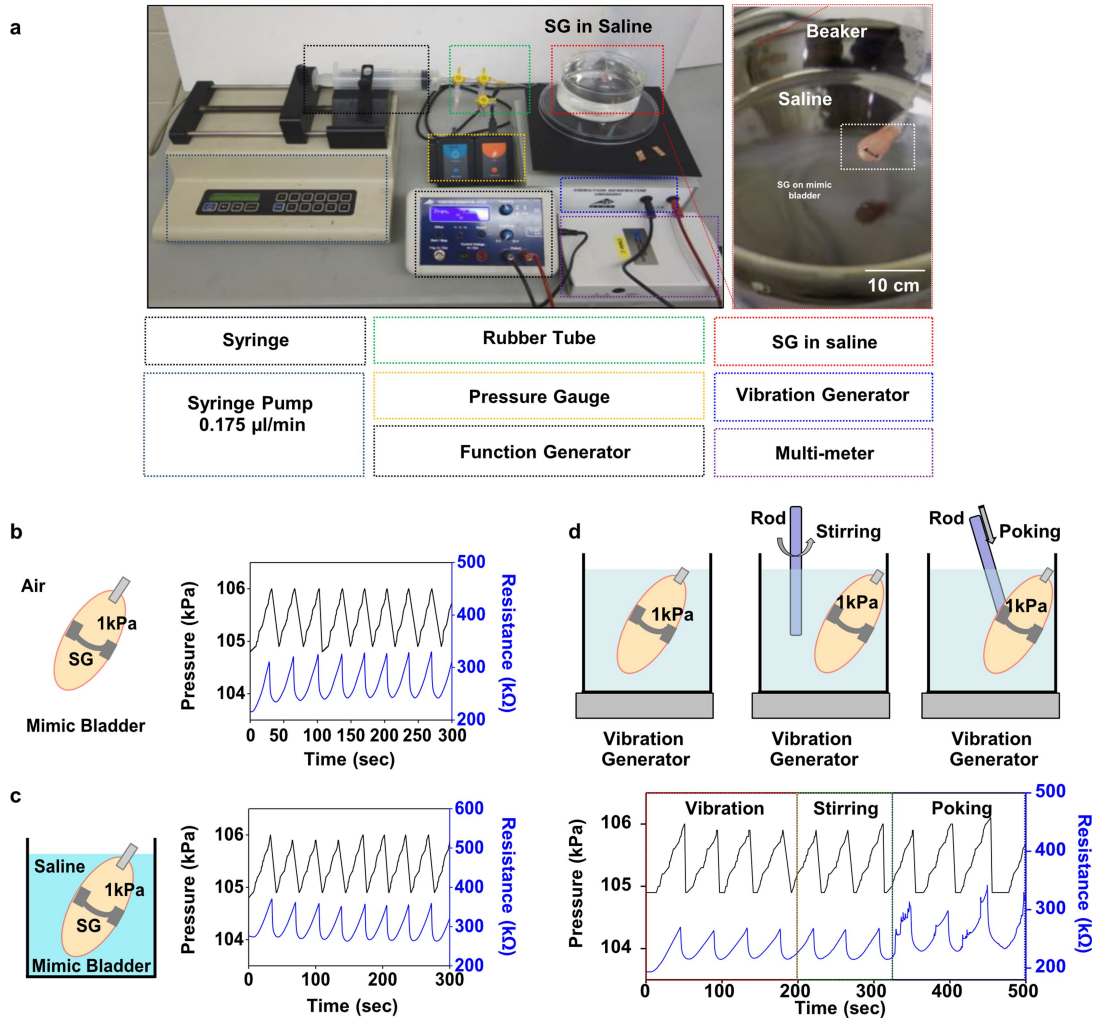
Extended Data Fig. 8 | Effect of Arch activation and CYP-induced bladder dysfunction on voiding properties. **a, b**, Representative traces (**a**) and grouped data (**b**) that demonstrate a significant increase in cystometric inter-contraction interval (ICI) during green light illumination in HSV-Arch-injected animals compared to HSV-eYFP-injected controls, as defined by the strain gauge and pressure recordings. $n = 4$ rats per group; unpaired t -test $*P < 0.05$. **c**, Activation of Arch in bladder sensory afferents does not affect base, threshold or peak pressure. No changes were observed during bladder illumination in base pressure, threshold pressure or peak pressure in anaesthetized (urethane) cystometry (0.1 ml min^{-1}) when comparing HSV-Arch-eYFP-injected rats to HSV-eYFP-injected rats. $n = 4$; unpaired t -test or Mann-Whitney test. **d**, Effect of Arch activation on normal voiding in awake, non-

anaesthetized rats. Illumination of HSV-Arch-injected bladders (Arch denotes HSV-Arch-eYFP/LED-ON) did not significantly alter the number of voids or time to first void compared to HSV-eYFP (eYFP denotes HSV-eYFP/LED-ON) and HSV-injected/No LED groups in non-inflamed animals. $n = 6$; two-way ANOVA with Tukey's multiple comparison test. **e**, Rats injected with CYP have significantly more voids and less time to first void during the 3 h after CYP injection as compared to baseline. $n = 6$; unpaired t -test or Mann-Whitney test, $**P < 0.01$. **f**, A single dose of CYP does not cause a significant increase in evoked VMR. $n = 8$ saline, $n = 9$ CYP; one-way ANOVA with Sidak's multiple comparisons test. All data mean \pm s.e.m (further statistical details can be found in Supplementary Table 1).



Extended Data Fig. 9 | Automatic identification of voiding events from raw strain gauge data. **a**, Diagram demonstrating the step-by-step process (top to bottom) for identifying voids from raw strain gauge data. **b**, Quantification of the number of missed voids, false voids, false voids per hour and per cent correct during 8 h of recording at baseline and 8 h after CYP injection using the void detection algorithm. $n = 9$ rats per group; mean \pm s.e.m. **c**, Per cent change in void size after CYP administration (75 mg kg^{-1}) ($n = 11$ biologically independent animals; mean \pm s.e.m.).

d, In vitro demonstration of the void volume threshold component of the closed-loop algorithm. With a threshold of 15 arbitrary units (AU) (20% fractional change of resistance), the closed-loop system did not activate when the void volumes were larger than 15 AU (right), while the closed-loop system was triggered and turned on the μ -ILEDs when void sizes were smaller than 15 AU (left). **e**, Demonstration of prolonged battery-free recording (repeated twice in independent animals with similar results).



Extended Data Fig. 10 | Results from in vitro testing of the strain gauge. **a**, Photograph of the in vitro setup, including a strain gauge on a mimic bladder (Ecoflex-0030) in saline solution (pH 7.4), a syringe pump ($0.175 \mu\text{l min}^{-1}$) to control the size of the bladder, a function generator to supply power (7 Hz, 10 V) for external vibration, a pressure gauge and a digital multimeter to monitor pressure in the bladder. **b**, Change in

resistance of the strain gauge on a mimic bladder during inflation at an inner pressure of 1 kPa, in otherwise ambient laboratory conditions. **c**, Similar changes during inflation with saline solution at 1 kPa. **d**, Change in resistance change of the strain gauge under the various conditions; vibration, stirring, and poking.